Cite this article as: Mancino S., et al. (2024). Exploring the Stability of Genomic Imprinting and X-Chromosome Inactivation in the Aged Brain, *AgingBio*, *2*, e20240030. doi: 10.59368/agingbio.20240030.

Research Paper

Exploring the Stability of Genomic Imprinting and X-Chromosome Inactivation in the Aged Brain

Samantha Mancino,[1,2,3,¶] Janith Seneviratne,[4,5,¶] Annalisa Mupo,[6,7] Felix Krueger,[7,8] David Oxley,[9] Melanie A. Eckersley-Maslin,[4,5,10,*] and Simão Teixeira da Rocha[1,2,3,*]

[1]Instituto de Bioengenharia e Biociências e Departamento de Bioengenharia, Instituto Superior Técnico, Universidade de Lisboa, Lisboa, Portugal
[2]Associate Laboratory i4HB—Institute for Health and Bioeconomy, Instituto Superior Técnico, Universidade de Lisboa, Lisboa, Portugal
[3]Faculdade de Medicina, Instituto de Medicina Molecular, João Lobo Antunes, Universidade de Lisboa, Lisboa, Portugal
[4]Peter MacCallum Cancer Centre, Melbourne, VIC, Australia
[5]Sir Peter MacCallum Department of Oncology, The University of Melbourne, Melbourne, VIC, Australia
[6]Epigenetics Programme, Babraham Institute, Cambridge, United Kingdom
[7]Altos Labs, Cambridge, United Kingdom
[8]Bioinformatics Group, Babraham Institute, Cambridge, United Kingdom
[9]Mass Spectrometry Facility, The Babraham Institute, Cambridge, United Kingdom
[10]Department of Anatomy and Physiology, The University of Melbourne, Melbourne, VIC, Australia
[*]Corresponding authors: melanie.eckersley-maslin@petermac.org; simao.rocha@tecnico.ulisboa.pt
[¶]Samantha Mancino and Janith Seneviratne have equally contributed to this research.

https://doi.org/10.59368/agingbio.20240030
Received: 9/29/2023, Revised: 4/11/2024, Accepted: 6/22/2024, Published: 7/31/2024

Changes in the epigenetic landscape are a hallmark of aging that contributes to the irreversible decline in organismal fitness ultimately leading to aging-related diseases. Epigenetic modifications regulate the cellular memory of the epigenetic processes of genomic imprinting and X-chromosome inactivation (XCI) to ensure monoallelic expression of imprinted and X-linked genes. Whether aging-associated epigenetic changes affect the maintenance of genomic imprinting and XCI has not been comprehensively studied. Here, we investigate the allele-specific transcriptional and epigenetic signatures of the aging brain, by comparing juvenile and old hybrid mice obtained from C57BL/6J (BL6) and CAST/EiJ (CAST) reciprocal crosses, with an emphasis on the hippocampus (HCP). We confirmed that the aged HCP showed an expected increase in DNA hydroxymethylation and a typical aging transcriptional signature. Importantly, genomic imprinting was largely unaffected, with stable parent-of-origin-specific DNA methylation in multiple brain regions including the HCP, cerebellum, nucleus accumbens, hypothalamus, and prefrontal cortex. Consistently, allele-specific transcriptomic bulk analysis confirmed unaltered imprinting expression in the aged HCP. An exception was four novel non-coding transcripts (*B230209E15Rik*, *Ube2nl*, *A330076H08Rik*, and *A230057D06Rik*) at the Prader-Willi syndrome/Angelman syndrome imprinted locus, which lost strict monoallelic expression during aging. Similar to imprinting, XCI was remarkably stable with no signs of aging-driven skewing or relaxation of monoallelic expression of X-linked genes. Our study provides a valuable resource for evaluating monoallelic expression in the aging brain and reveals that, despite the known epigenetic changes occurring during aging, genomic imprinting and XCI remain predominantly stable throughout the process of physiological aging in the mouse brain.

Introduction

Aging can be defined as an irreversible loss of physiological integrity associated with the functional decline of tissues and organs, progressively leading to aging-related illnesses, such as neurodegenerative diseases[1]. At the molecular and cellular levels, several hallmarks have been associated with aging, including changes in the epigenetic landscape[2,3]. DNA methylation is affected by these aging-related epigenetic changes. Here, cytosine Bases followed by guanine, known as CpG sites, can acquire a methyl group at the C-5 position (5-methylcytosine [5mC]). Some regions of the genome can undergo age-induced gains and losses in DNA methylation, and these changes can condition their pattern of gene expression[4]. This pattern of DNA methylation changes during lifespan can be used as an "epigenetic clock" to predict chronological age[5,6]. This phenomenon indicates that challenges in preserving epigenetic marks may lead to changes in accessibility and gene expression patterns that, in turn, impact the cellular and molecular functions of aged cells[5].

Neurons, as long-lived post-mitotic cells in the brain, are characterized by an evolving epigenetic landscape during differentiation, maturation, and aging, making them a prime target for studying

cellular aging in the context of brain function and health[7–11]. Disease signatures based on DNA methylation patterns have also been linked to a variety of age-related neurological and psychiatric disorders[12–15]. 5mC can be catalyzed to 5-hydroxymethylcytosine (5hmC) by the ten-eleven translocation (Tet) family of dioxygenases as a part of the active DNA demethylation cycle. While much less abundant than 5mC, 5hmC levels are particularly high in the adult brain when compared with other somatic tissues[10] and accumulate during aging[16–18]. The precise significance of 5hmC in the brain and its accumulation during lifespan has been postulated to result from enhanced DNA demethylation activity necessary for the epigenetic regulation of brain-specific genes involved in neurodevelopmental processes and neuronal function and plasticity[19]. The dynamic changes in 5mC and 5hmC in the brain are illustrative of the different layers of complex epigenetic regulation used by neurons and other brain cells to integrate signals and outputs underlying highly skillful processes such as learning and memory.

Epigenetic mechanisms, such as DNA methylation, are main actors in the regulation of monoallelic expression of genes, playing a crucial role in the establishment and/or maintenance of the mammalian epigenetic processes of genomic imprinting and X-chromosome inactivation (XCI)[20]. Many genes regulated by these processes have critical roles in brain development and function and are thought to contribute to the diversity and specialization of neuronal cells[21]. Whether aging-associated epigenetic changes affect the heritability of monoallelic expression during physiological aging and impact the aging process remains an open question.

Imprinted genes consist of a unique subset of ~150 genes displaying parental-of-origin-specific gene expression. The majority are located in ~25 genomic clusters where their monoallelic expression is dependent on DNA methylation at CpG-dense regulatory regions, known as imprinting control regions (ICRs)[22]. This DNA methylation is asymmetrically deposited during female and male germline development. Interestingly, a substantial number of imprinted genes exhibit monoallelic or biased expression from one parental allele in one tissue or at specific developmental stage[23,24]. In this regard, the brain is one of the organs where more genes show tissue-, isoform-, or developmental-stage-specific imprinting[25–27]. Within the brain, this is highly regionalized, with different areas exhibiting their own set of monoallelic or parentally biased expressed genes[26,28]. The importance of imprinted genes in brain function is evidenced by the devastating neurological and behavioral conditions such as Angelman and Prader-Willi syndromes resulting from (epi)mutations affecting the chr15q11-q13 region in humans[29]. Transcriptomic studies have shown that imprinting expression in the cerebellum (CB) is developmentally regulated[25]. Whether imprinting is also susceptible to changes as a function of aging has not been systematically addressed.

XCI is a dosage compensation mechanism that equalizes X-linked gene expression of XX females to XY males[30]. This process is established early in development and is regulated by the *X-inactive-specific transcript* (*XIST*) long non-coding RNA (lncRNA). During embryogenesis, *XIST* is upregulated randomly from one of the two X chromosomes and becomes exclusively expressed from the inactive X chromosome (Xi). This lncRNA engages in a complex interplay with several RNA-binding proteins to recruit transcriptional repressors and chromatin modifiers, establishing the silenced state of the Xi[31,32]. Although the molecular mechanisms underlying the initiation of XCI have been extensively elucidated, our understanding of the long-term maintenance of XCI throughout an organism's lifespan remains limited. Recent investigations in aging, with a focus on the hematopoietic cell lineage, reveal an escalation in XCI skewing, where one parental allele is preferentially inactivated[33] along with subtle alterations in DNA methylation patterns and gene expression across the X chromosome[34,35]. Interestingly, a separate study conducted in the brain, employing single nuclei transcriptomics, unveiled an intriguing finding: *Xist* expression is observed to be upregulated in aged neurons located within the hypothalamus and hippocampus (HCP) of female mice[36]. The implications of this observation on XCI remain ambiguous, underscoring the necessity for in-depth investigations to elucidate the influence of aging on XCI within the context of the brain.

In the present study, we provide the first allele-specific epigenetic and transcriptional landscape of the aging mouse brain. We particularly focus on the HCP, a key regulator brain area of cognitive processes that tend to decline during aging. We used juvenile (8–9 weeks) and old (>100 weeks) F1 hybrid mice from reciprocal crosses between distantly related mouse strains to gain allelic resolution. DNA methylation and transcriptomic analysis enabled us to discern the impact of aging on monoallelic expression in the brain. Our results support the stable epigenetic inheritance of genomic imprinting and XCI during physiological aging of the mouse brain.

Materials and Methods

Ethics

Animal welfare and experimental procedures were conducted according to the ethical guidelines of the European Directive 2010/63/EU and the Portuguese legislation DL 113/2013 and were approved by the responsible Ethical Committee of Instituto de Medicina Molecular João Lobo Antunes (iMM) and the Portuguese competent authority, Direção Geral de Alimentação e Veterinária (license number 023357/19).

Animals

Mice colonies of *Mus musculus* C56BL/6J (BL6) strain and *Mus musculus castaneus* CAST/EiJ (CAST) strain were obtained from the Jackson Laboratory and maintained at the iMM Rodent facility. Animals were housed in a maximum of five per cage in a temperature- and humidity-controlled room (24°C, 45%–65%) with a 14/12 hour light/dark cycle. Animals were fed diet *ad libitum*.

Reciprocal crosses between BL6 and CAST animals—BL6/CAST (BL6 female and CAST male) and CAST/BL6 (CAST female and BL6 male) were established to generate F1 animals. Juvenile and old F1 animals were developed and sacrificed by cervical dislocation in the range of 8–9 weeks and 102–104 weeks, respectively. A total of 10 young female (six BL6/CAST and four CAST/BL6), four young male (two BL6/CAST and two CAST/BL6), seven old female (five BL6/CAST and two CAST/BL6), and five old male (two BL6/CAST and three CAST/BL6) were used in this study (**Table S1**). Female mice were not synchronized for the estrous cycle.

Samples preparation

Sacrificed animals were decapitated by cervical dislocation. The brains were quickly removed and the whole CB and hypothalamus were rapidly isolated from the brainstem. The following brain areas were then dissected according to the atlas of stereotaxic coordinates of mouse brain[37] and immersed in liquid

nitrogen for 4 sec: HCP (from bregma, Anterior/Posterior [AP]: from −1.34 to −2.56 mm; Medial/Lateral [ML]: ±0 mm; Dorsal/Ventral [DV]: −3 mm), medial prefrontal cortex (from bregma, AP: from −2.10 to −1.70 mm; ML: ±0 mm; DV: −3.5 mm), and nucleus accumbens (from bregma, AP: from −1.54 to −0.98 mm; ML: ±0.5 mm; DV: −4 mm). Lung tissue was also collected. After collection, brain areas and lung tissue were immediately frozen in liquid nitrogen and stored at −80°C for later molecular analysis. DNA and RNA were isolated for each brain area or lung tissues from the selected animal tissues using the NucleoSpinTriPrep kit (Cat# 740966.50, Macherey-Nagel GmbH & Co.KG, Germany) according to the manufacturer's guidelines.

5mC/5hmC measurements by liquid chromatography–mass spectrometry (LC-MS/MS)

Genomic DNA from the CB, HCP, and lung of both juvenile and old female mice was digested using DNA Degradase Plus (Cat# E2020, Zymo Research) according to the manufacturer's instructions. Nucleosides were analyzed by LC-MS/MS on a Q-Exactive mass spectrometer (Thermo Scientific) fitted with a nanoelectrospray ion source (Proxeon). All samples and standards had a heavy isotope-labeled nucleoside mix added prior to mass spectral analysis (2′-deoxycytidine-$^{13}C_1$, $^{15}N_2$ [Cat# SC-214045, Santa Cruz], 5-(methyl-$^{2}H_3$)-2′-deoxycytidine [Cat# SC-217100, Santa Cruz], 5-(hydroxymethyl)-2′-deoxycytidine-$^{2}H_3$ [Cat# H946632, Toronto Research Chemicals]). MS2 data for 5hmC, 5mC, and C were acquired with both the endogenous and corresponding heavy-labeled nucleoside parent ions simultaneously selected for fragmentation using a 5 Th isolation window with a 1.5 Th offset. Parent ions were fragmented by higher-energy collisional dissociation with a relative collision energy of 10% and a resolution setting of 70,000 for MS2 spectra. Peak areas from extracted ion chromatograms of the relevant fragment ions, relative to their corresponding heavy isotope-labeled internal standards, were quantified against a six-point serial twofold dilution calibration curve, with triplicate runs for all samples and standards.

Bisulfite treatment

Genomic DNA (1 μg) from the CB, HCP, hypothalamus, medial prefrontal cortex, nucleus accumbens, and lung of four juvenile and four old female mice (two animals for each reciprocal cross) was bisulfite converted using the EZ DNA methylation Gold kit (Cat# D5006, Zymo Research) according to the manufacturer's instructions. After column cleanup, the DNA was eluted in an elution buffer (66 μl) to obtain a final concentration of ∼15 ng/μl bisulfite converted DNA.

IMPLICON library preparation and analysis

IMPLICON was performed as previously described[38] for the CB, HCP, nucleus accumbens, prefrontal cortex, hypothalamus, and lung of four juvenile and four old female mice (two animals for each reciprocal cross). Briefly, following bisulfite conversion, a first polymerase chain reaction (PCR) amplifies each region per sample in individual reactions, adding adapter sequences, as well as eight random nucleotides (N_8) for subsequent data deduplication. PCR conditions and primers for this first step are listed in **Table S2**. Primers cover 11 imprinted clusters (10 ICRs and exon1a promoter of *Ddc* gene), together with two unmethylated (*Sox2, Klf4*) and one methylated (*Prickle1*) control regions. After pooling amplicons for each biological sample and clean-up using AMPure XP magnetic beads (Cat# A63880, Beckman Coulter), a second PCR completes a sequence-ready library with sample barcodes for multiplexing. In this PCR reaction, barcoded Illumina adapters are attached to the pooled PCR samples ensuring that each sample pool receives a unique reverse barcoded adapter. Libraries were verified by running 1:30 dilutions on an Agilent bioanalyzer and then sequenced using the Illumina MiSeq platform to generate paired-end 250 bp reads using the indexing primer with the following sequence, 5′-AAGAGCGGTTCAGCAGGAATGCCGAGACCGATCTC-3′ and 10% PhIX spike-in because the libraries are low complexity. We run two independent IMPLICON libraries that were named: first run (lane 7651) and second run (lane 7950). The first run contained the CB, HCP, nucleus accumbens, prefrontal cortex, hypothalamus, and lung of four juvenile and four old female mice, while the second run contained the samples of CB, HCP, and lung of the same mice.

IMPLICON bioinformatics analysis was also performed as described previously[38], following the step-by-step guide of data processing analysis in https://github.com/FelixKrueger/IMPLICON. Briefly, data were processed using standard Illumina base-calling pipelines. As the first step of processing, the first 8 bp of Read 2 were removed and written into the readID of both reads as an in-line barcode or unique molecular identifier (UMI). This UMI was then later used during the deduplication step with "deduplicate bismark barcode mapped_file.bam." Raw sequence reads were then trimmed to remove both poor-quality calls and adapters using Trim Galore v0.5.0 (www.bioinformatics.babraham.ac.uk/projects/trim_galore/, Cutadapt version 1.15, parameters: –paired). Trimmed reads were aligned with the mouse reference genome in paired-end mode. Alignments were carried out with Bismark v0.20.0. CpG methylation calls were extracted from the mapping output using the Bismark methylation extractor. Deduplication was then carried out with deduplicate_bismark using the barcode option to take UMIs into account (see above). The data were aligned with a hybrid genome of BL6/CAST (the genome was prepared with the SNPsplit package v0.3.4 [https://github.com/FelixKrueger/SNPsplit]). Following alignment and deduplication, reads were split allele specifically with SNPsplit. Aligned read (.bam) files were imported into Seqmonk software v1.47 (http://www.bioinformatics.babraham.ac.uk/projects/seqmonk) for all downstream analysis. Probes were made for each CpG contained within the amplicon and quantified using the DNA methylation pipeline or total read count options. Downstream analysis was performed using Microsoft Excel spreadsheet software (v2206 Build 16. 0. 15330. 20144) and GraphPad Prism v8.0.1.

From the raw data deposited in gene expression omnibus (GEO) under the accession number GSE148067, the reads mapped to the following murine (mm10) genomic coordinates were excluded from consideration in this article for one of the following reasons: (1) regions that fail to reach the coverage threshold for the two parental alleles in a given sample (>50 reads), including 3 of 13 imprinted regions, *Igf2-H19*, *Igf2r*, and *Grb10,* presented in our original IMPLICON primer set[38]; (2) regions sequenced twice for which only the run with more reads was considered; and (3) regions out of the scope of this article. For the samples sequenced in lane 7651, this includes: Chr7:60005043-60005284, Chr7:142581761-142582087, Chr12:109528253-109528471, Chr6:30737609-30737809, Chr11:12025411-12025700, and Chr18:12972868-12973155; for the samples sequenced in lane 7950, this includes: Chr7:142581761-142582087, Chr7:142659774-142664092, and Chr11:12025411-12025700.

RNA sequencing

The quality of DNAse I-treated total RNA from female young and old hippocampi (n = 5 old mice: n = 2 CAST-BL6 and n = 3 BL6-CAST; n = 6 young mice, n = 3 of each reciprocal cross) was checked by 2100 Agilent Bioanalyser. Samples with RNA integrity number (RIN) score above 9 were processed. RNA (1 μg) was used as input for PolyA+ directional RNA-seq library preparation using the NEBNext Ultra II Directional RNA-seq Kit (#E7765, NEB) with the PolyA mRNA magnetic isolation module (#E7490, NEB) according to the manufacturer's instructions. The pooled library was sequenced on an Illumina HiSeq 2000 with a 2 x 100 bp kit.

Fastqs were processed using TrimGalore v0.6.6 in paired-end mode with default parameters. Validated read pairs were then aligned with the GRCm38.v5 mouse genome using Hisat2 v2.1.0 with the following parameters: –dta, –no-softclip, –no-mixed, and –no-discordant. The resulting hits were filtered to remove mappings with Mapping Quality (MAPQ) scores of < 20 and then converted to BAM format using Samtools v1.10. Allele-specific alignments were also performed by realigning mapped reads to N-masked genomes C56BL/6 J (genome 1) and CAST/EiJ (genome 2), which was based on the GRCm38.v5 genome and generated using the SNPsplit v0.3.4 package. Reads that were then sorted by allele-specificity for either genome or reads containing conflicting Single Nucleotide Polymorphism (SNP) information were excluded. Total and allele-specific read counts were quantified from BAMs with feature counts (from the subread v2.0.0 package) using default parameters with gencode vM25 annotations. Basic statistics on read counts and mappability are provided in **Table S3**.

We used SNP information to measure allele-specific expression (ASE) and performed DESeq2 analysis between maternal and paternal alleles, excluding those genes that exhibited random (i.e., genes with monoallelic expression independent of parental origin or strain) or strain-dependent (i.e., all genes with biased expression according to the genetic background) monoallelic expression.

DESeq2 v1.34.0 package in an R (v4.1.2)/R Studio (v2022.02.0 +443) environment was used thus for conducting all differential gene expression analyses (including total and allele-specific analyses). For all analyses (including gene level), low expressed genes were first filtered (genes with ≥ 10 read counts across both alleles in each sample and ≥ 1 TPM in each sample across all samples were kept). For allele-specific analyses, allelic ratios were first derived by dividing the maternal or paternal allele counts by the total number of allelic counts (ratios are between 0 and 1). These allelic ratios were then used as input into DESeq2 after adjusting size factors to 1 for each sample (to account for allelic ratio input). To determine ASE (either maternal or paternal) across all mice, a DESeq design (~0 + age + genome + sample + allele) was used with blocking terms against age group and the genome of origin for each allele to reduce the impact of age- or cross-specific allelic expression. To determine ASE (either maternal or paternal) in young and old mice separately, a separate DESeq2 design (~0 + genome + age + age:sample + age:allele) was used. Contrasts were then made between old and young mice to determine age-specific and ASE changes that were attributed to age. Genes with ASE were considered as those with an absolute log2FoldChange > 1 and adjusted p-value (Benjamini–Hochberg adjusted) < 0.05. For calculating the proportion of reads aligning to the mouse genome, aligned reads on ChrX were counted from BAMs using feature counts either in an allele-specific context (post-SNPsplit for BL6 and CAST alleles) or allele-independent context (pre-SNPsplit). These counts were then divided by the total number of aligned reads and multiplied by 10^6 to obtain ChrX reads per million. ChrX count proportions for the BL6 allele were determined by dividing BL6 counts on ChrX by the total read counts on ChrX across both alleles (post-SNPsplit).

Principal component analysis (PCA) was conducted using the *prcomp* function from the stats v4.1.2 R package using DESeq2 normalized counts for all genes. Barplots, boxplots, and volcano plots were plotted using the ggplot2 v3.3.5 R package, and heatmaps were constructed using the ComplexHeatmap v2.10.0 R package. The genomic distribution of imprinted genes on chromosomes was plotted using the karyoplotR v1.20.3 R package. Track plots of normalized read densities (for RNA-seq data) were plotted for several genomic loci of interest using the rtracklayer v1.54.0 and Gviz v1.38.4 R packages.

For the analysis of the bulk HCP dataset from Hahn et al.[39], raw gene counts were obtained from GEO under the accession number GSE212336. This dataset was subsetted for samples originating from female mice hippocampi (both posterior and anterior sites) for comparison with the data generated in this study. In this comparison, young mice were considered to be 3 months old, while old mice were considered to be 21 months old. These are the timepoints that better match our young (~2 months) and old (~24 months) animals. We performed differential gene expression analyses between old and young mice in this dataset using DESeq2 with a design (~anatomical_site + age) and the same thresholds for statistical significance as above was considered (absolute log2FoldChange > 1, BH-adjusted p-value < 0.05). Heatmaps for these data were plotted for various genes using ComplexHeatmap, wherein DESeq2 normalized counts were subject to z-score normalization across samples within the same tissue type prior to plotting (note for the heatmap, animals of 12, 15, and 18 months old from Hahn's dataset were also considered). To summarize gene expression signatures (upregulated and downregulated), the mean of z-score normalized values across the relevant genes for each signature was taken. Column graphs for various genes were plotted for these data using ggplot2.

CIBERSORTx analysis

Single-cell RNA-seq datasets in the form of UMI count matrices were retrieved for the hippocampi of four mice (two young and two old) from GEO under the accession number GSE161340[40]. Matrices were loaded and processed using the Seurat v4.2.0[41] R package (*Read10X* > *CreateSeuratObject* > *merge*). The fraction of reads aligned to mitochondrial (*mt-*) or ribosomal (*Rps|Rpl|Mrps|Mrpl*) genes out of all reads was calculated for each cell using *PercentageFeatureSet*. Cells were quality filtered for the UMI counts (100 < n < 20000), number of genes expressed (200 < n < 6000), mitochondrial read (<0.1), and ribosomal read (<0.5) fractions. Data were then subjected to normalization and scaling using *SCTransform* with the top 3000 variable genes. PCAs (*RunPCA*), mutual nearest neighbors (*FindNeighbors,* top 30 principal components), Uniform Manifold Approximation and Projection (UMAP) dimensional reduction (*RunUMAP*), and clustering (*FindClusters*, resolution = 1) were then performed. Gene signatures were constructed using canonical cell type marker genes defined in a comparative scRNA-seq study of mouse hippocampi in the literature[42]. Module scores that summarize the gene expression of canonical gene signatures among cell types were then computed using *AddModuleScore*. Violin plots were plotted using *VlnPlot.* Cell type classifications were made per cell cluster, wherein median cell type signature scores surpassing 0 were used to assign a given cell type. For

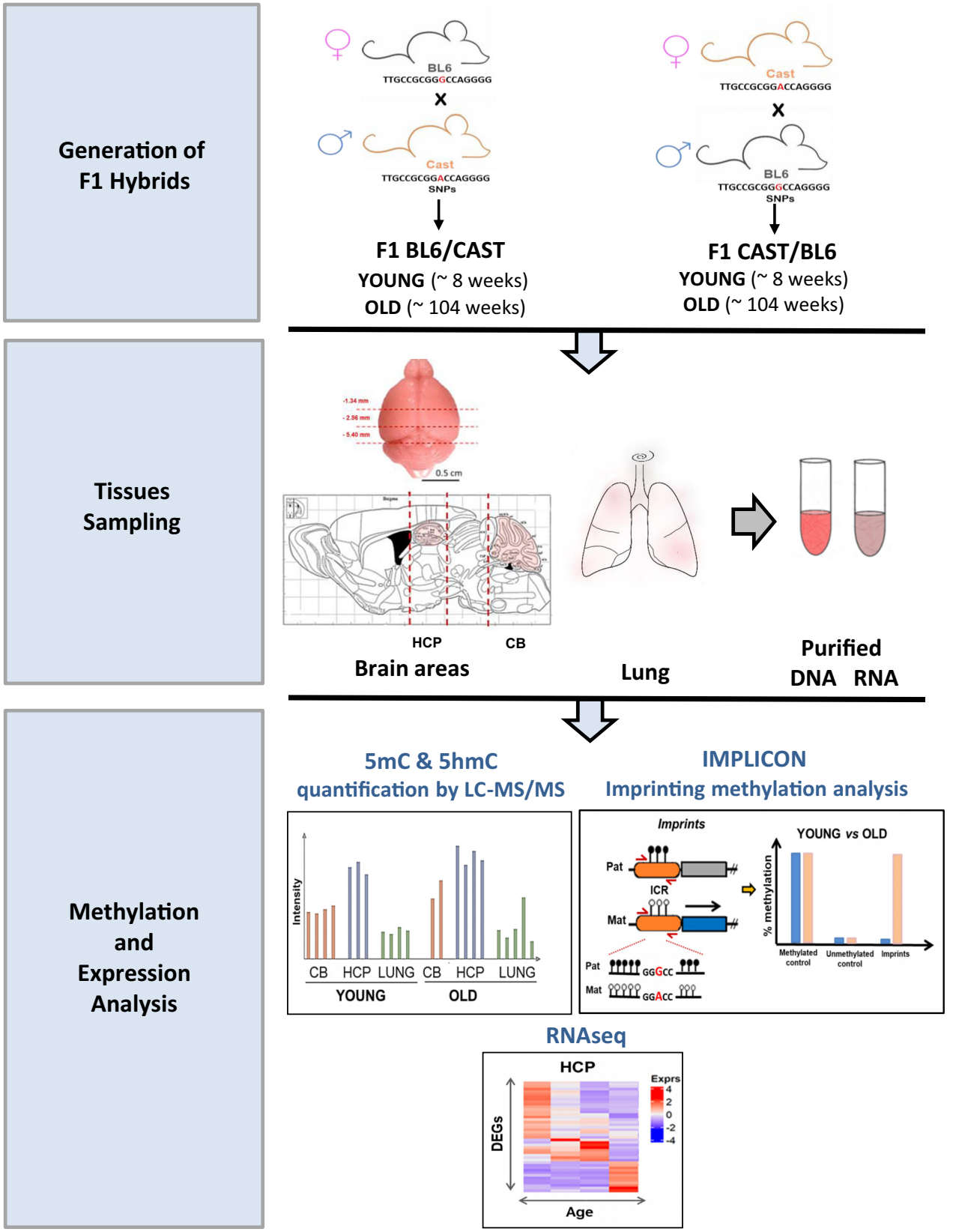

Figure 1. Workflow of the allele-specific methylation/transcriptional profiling of the aging brain. First, F1 hybrid mice were generated by crossing C57BL/6J (BL6) females with Cast/EiJ (CAST) males (BL6/Cast) and reciprocally crossing CAST females with BL6 males (CAST/BL6) and aged for ~8 weeks (YOUNG) and ~104 weeks (OLD). Second, young and old mice were sacrificed, and specific tissues were dissected such as hippocampus (HCP), cerebellum (CB), and lung. For dissection of the brain areas, stereotaxic coordinates of the mouse brain were used[37]. Dissection planes (red dotted lines)

(legend continued on next page)

on brain tissue are shown on a sagittal view of a mouse brain from the Paxinos atlas; regions are not drawn to scale. Both DNA and RNA were extracted from the tissues and purified. Third, we perform the methylation and transcriptional profiling of young and old tissue samples, by measuring global methylation levels, both 5-methylcytosine (5mC) and 5-hydroxymethylcytosine (5hmC) using liquid chromatography with tandem mass spectrometry (LC-MS/MS), by profiling allele-specific methylation at imprinting regions using IMPrintampLICON (IMPLICON) and assessing allele-specific expression (ASE) by RNA sequencing (RNAseq).

deconvolution analyses, each cell type was randomly downsampled to 100 cells (*sample* and *subset*). Downsampled raw UMI count matrices with cell type annotations were further subsetted for genes commonly expressed in our bulk RNA-seq dataset. This matrix was then input to CIBERSORTx[43] (https://cibersortx.stanford.edu/) as a single-cell reference matrix, wherein a signature matrix was first derived to determine those genes that accurately predicted each cell type (replicates [100], sampling [0.5], and fraction [0.0]). Cell fractions were then imputed for the HCP samples derived in this study (raw counts) using the aforementioned signature matrix with CIBERSORTx, without batch correction. Imputed cell fractions for each sample were then plotted using the ggplot2 R package. Cell type proportions in old and young mice were compared using pairwise t-tests (BH adjusted to account for multiple comparisons).

We also analyzed single-cell RNA-seq data for Fluorescence-Activated Cell Sorting (FACS)-sorted whole mouse brains (both myeloid and non-myeloid cell types) from the Tabula Muris Senis study, which profiled several whole young and old mouse brains[44]. The pre-processed RNA-seq counts containing 17 cell type annotations for cell types identified in brain tissues contained within the TabulaMurisSenisData R package (v1.0.0) were used as input to CIBERSORTx to first derive a signature matrix (replicates [15], sampling [0.5], and fraction [0.0]). Cell fractions were then imputed for the HCP samples derived in this study with the aforementioned signature matrix using CIBERSORTx.

Statistics

Statistical analysis used for each experiment is indicated in the respective figure legend with p-values indicated or marked as *p-value < 0.05, **p < 0.01, and ***p < 0.001. According to the distribution of data analyzed by the Shapiro–Wilk test, the following tests for the differential analysis of the experiments were used: unpaired two-tailed Welch's t-test (**Fig. 2A**), two-way ANOVA followed by Tukey's multiple comparisons test (**Fig. 3B,C**; **Fig. S3A**), three-way ANOVA by Tukey's multiple comparisons test (**Fig. S3B**, for the cross), and Kruskal–Wall by Dunn's multiple comparisons test (**Fig. S1A,B**). Differential (allelic or non-allelic) expression analysis of RNAseq data was conducted using DESeq2 package. Comparisons were considered statistically significant after a Wald test with Benjamini–Hochberg adjustment of p-values to account for multiple comparisons when adjusted p-values were < 0.05 and absolute log2FoldChange > 1. For the gene set enrichment analysis (GSEA) of differentially expressed genes (DEGs), the log adj p-value for each enriched gene set and normalized enrichment score (NES) were considered for the analysis (**Fig. 2Cii**; **Fig. S2**).

Results

Increase in 5hmC levels is a hallmark of the aging HCP

To decipher the allele-specific epigenetic and transcriptional features of the aging brain, we established reciprocal crosses between BL6 and CAST mice to generate female and male BL6-CAST and CAST-BL6 F1 hybrid mice (**Fig. 1**). The use of F1 hybrid mice from genetically distant murine strains allows the distinction of parental alleles based on frequent genetic variants on regulatory regions and genes. The use of reciprocal crosses allows for the distinction between parent-of-origin and genetic allelic effects[25,45]. These mice were sacrificed at 8–9 weeks (young) and > 100 weeks (old) of age and different brain areas as well as other organs were collected for DNA methylation and transcriptomic analyses (**Fig. 1**; **Table S1**). We concentrated our study on the HCP and the CB, which are important regions for cognitive function often impaired during aging, with the lung used as a non-brain control.

We first evaluated the overall levels of 5mC and 5hmC by LC-MS/MS in young and old tissues from female and male animals of both reciprocal crosses (**Table S1**). 5mC levels did not differ significantly among CB, HPC, and lung and were not affected by age (**Fig. 2Ai**). In contrast, 5hmC levels were higher in neuronal tissues, especially in the HPC, where it increased further with aging (**Fig. 2Aii**), independent of the direction of the cross or biological sex (**Fig. S1A,B**; **Table S4**). This corroborates previous results on aging-induced increase in 5hmC levels[17,46] and confirmed that increase in 5hmC is a hallmark of the aged HCP.

Transcriptomic signatures of the aged HCP

We next examined alterations in the transcriptome occurring during aging of the HCP by employing RNAseq on samples obtained from both young and old mice. We selected the HCP due to the increase in 5hmC levels associated with aging. Specifically, we performed RNAseq analysis of female HCP, comprising a total of five samples from aged mice (two CAST-BL6 and three BL6-CAST individuals) and six samples from young mice (three individuals from each reciprocal cross). Clustering using PCA did not distinguish between mice of opposite reciprocal crosses, yet the combination of PC1 and PC2 was able to separate old and young mice (**Fig. S2A**). This dataset was thoroughly scrutinized to assess shifts in the expression of genes associated with the DNA methylation machinery over the aging process as well as to investigate the broader patterns of gene expression changes.

To better understand the cause leading to the increase in 5hmC levels upon aging, we first analyzed expression levels of the Tet methylcytosine dioxygenases (*Tet1*, *Tet2*, and *Tet3*) responsible for the sequential conversion of 5mC to 5hmC, and subsequent oxidation steps as a part of the active DNA demethylation pathway[47]. No differences were observed for any of the three *Tet* genes by RNAseq in HCP upon aging (**Fig. 2Bi**). Likewise, no differences in the DNA methyltransferase genes (*Dnmt1*, *Dnmt3a*, *Dnmt3b,* and *Dnmt3l* cofactor), responsible for catalyzing the transfer of a methyl group to DNA, were observed between young and old HPC (**Fig. 2Bi**). Curiously, a significant drop in *Uhrf1* mRNA expression, a gene encoding for a DNMT1-interacting protein essential for maintenance of methylation through DNA replication[48], was observed in the aged HPC (**Fig. 2B**). *Uhrf1* downregulation was not associated with measurable changes in 5mC levels perhaps because aged HPC is composed mostly by postmitotic cells. Overall, we rule out that the core DNA methyl/hydroxymethyl machinery is affected by aging.

Next, to conduct a broader analysis of gene expression, we performed differential gene expression analysis that identified

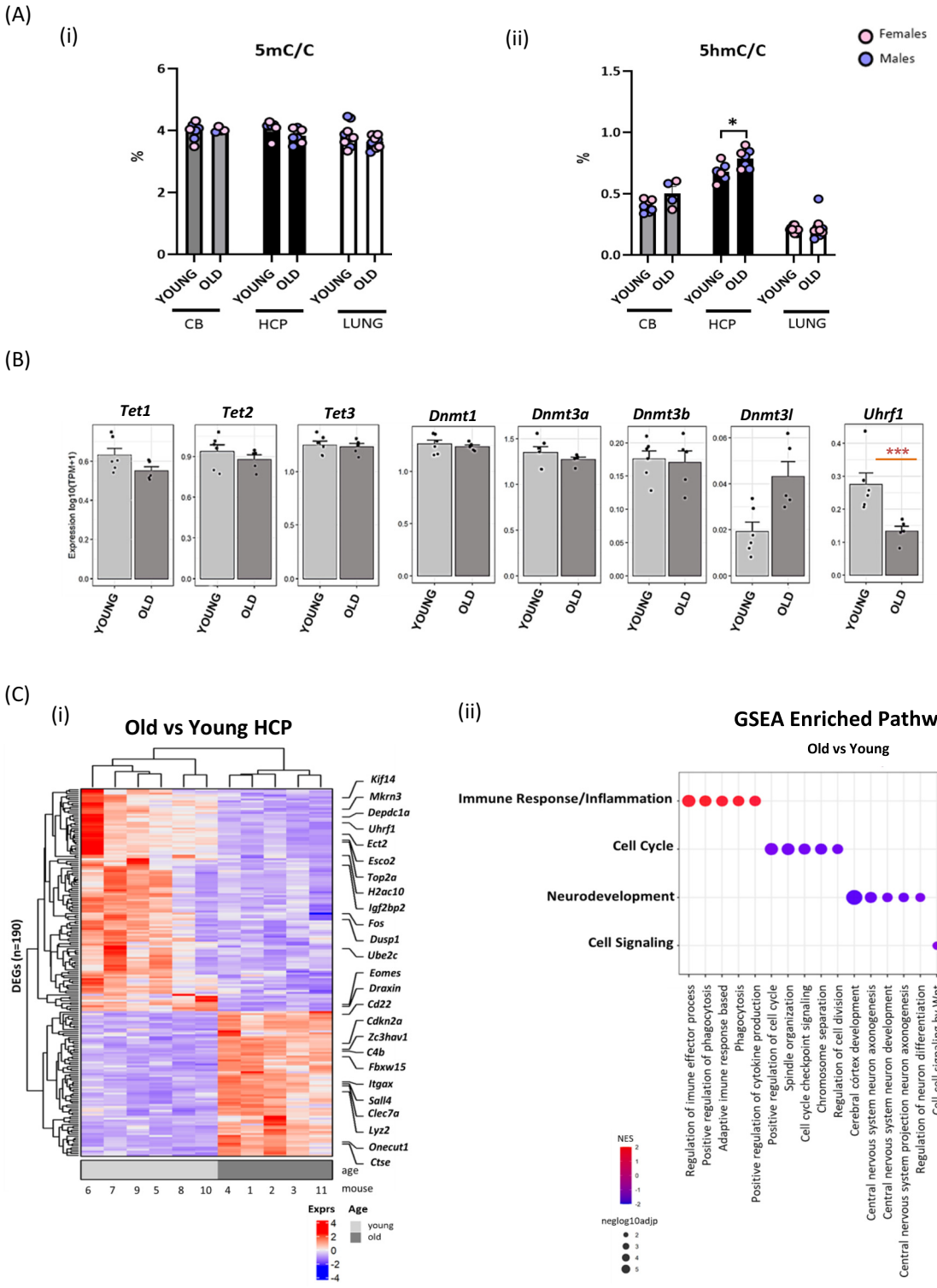

Figure 2. Global methylation and transcriptomic signatures of the aging brain. (A) (i) Global 5mC and **(ii)** 5hmC levels measured by LC-MS/MS in CB, HCP, and lung of young and old female and male F1 mouse hybrids from reciprocal crosses between C57Bl/6J (BL6) and Cast/EiJ (CAST) strains. Barplots represent the average percentage of 5mC or 5hmC ± standard error of the mean (SEM) of the total cytosines (C) for each three tissues. Individual values are represented by dots and male (blue) and female (pink) mice are distinguished by colors (CB: female n = 5 of which three young and two old, male n = 6 of which four young and two old; HPC: female n = 6 of which three young and three old, male n = 7 of which three young and four old; and lung: female n = 10 of which five young and five old, male n = 10 of which five young and five old). Statistically significant differences are indicated as *p-value < 0.05 between young and old mice per tissue (unpaired t-test, Welch's correction). **(B)** Expression levels of DNA methylation/hydoxymethylation-related genes, *Tet1*, *Tet2*, *Tet3*, *Dnmt1*, *Dnmt3a*, *Dnmt3b*, and *Uhrf1* measured by RNAseq. Barplots represent the average log10(TPM + 1) expression levels ± SEM of the different genes in young and old female HCP (n = 6 young mice; n = 5 old mice). Statistically significant differences determined by DESeq2 (Wald tests with BH adjustment of p-values to account for multiple comparisons) are indicated as ***adjusted p-value < 0.05 and

(legend continued on next page)

|log2 (fold-change)| >1. **(C)** Transcriptional phenotypes of the aging HCP in mice. Heatmap plot of the differentially expressed genes (DEGs) of young versus old hippocampi. Horizontal axis represents each mouse number ordered by age (light gray: young, total of six female mice; dark gray: old, total of five female mice). DEGs (n = 190 genes) determined by DESeq2 (Wald tests with BH adjustment of p-values) were selected by adjusted p-value < 0.05 and |log2 (fold-change)| >1. Gradient of color from red to blue, denotes, respectively, up- and downregulated DEGs in young versus old HCP. **(i)** Examples of genes that are UP or DOWN are shown on the right side of the heatmap. **(ii)** Dot plot showing representative GSEA pathways that were highly enriched within ontology gene sets using DEGs determined above (M5 pathway collection from the mouse Molecular Signatures Database [MSigDB]). Pathways are grouped into four groups where dot size represents the -log adj p-value for the enriched gene set. NES > 0 (red) indicates pathways enriched in old mice and NES < 0 indicates depleted pathways in old mice (blue).

75 upregulated and 115 downregulated genes during aging process (adjusted *p*-value [*P* adj] < 0.05, absolute log2 fold change [FC] > 1) (**Fig. 2Ci**; **Table S5**). Within the set of upregulated genes, we observed the presence of genes associated with cell cycle inhibition, such as *Cdkn2a*, as well as several genes involved in immune response and inflammation, such as *Cd22*, *Clec7a*, *Ctse*, *Lyz2*, and *C4b*. Accordingly, previous single-cell RNAseq analyses also identified *Lyz2* as an aging marker of microglia and *C4b* as an aging marker of astrocytes[36]. Downregulated genes were involved in cell cycle progression and chromosome segregation (e.g., *Kif4*, *Ect2*, *Esco2,* and *H2ac10*), regulation of transcription (e.g., *Fos* and *Top2a*), and neural development (e.g., *Eomes* and *Draxin*).

We validated the transcriptomic differences between young and old HCP by comparing it with a comprehensive dataset that profiled 847 brain samples (spanning 15 anatomical regions and taken from mice of varying ages between 3 and 28 months)[39]. Of relevance to our study were samples from the anterior and posterior HCP from 3, 12, 15, 18, and 21 months old female mice. We compared the expression of all DEGs between young and old HCP in our study in the anterior and posterior HCP from these female mice and observed gene expression trends that aligned with the direction of our DEGs, as shown by average z-score plots (**Fig. S2B**). We next specifically assessed DEGs between 3- and 21-month-old samples in this dataset to assess the level of overlap with our dataset. For this analysis, anterior and posterior HCP samples were analyzed together to increase the power of comparisons between age groups and not to miss any pan-HCP changes that we likely observe in our dataset. There were 44 up- and 2 downregulated genes (adjusted p-value < 0.05 and absolute log2FC > 1) in the Hahn et al. dataset[39] of which 13 upregulated genes (*Lyz2*, *C4b*, *Spag6*, *Lcn2*, *Bcl3*, *Cd22*, *Itgax*, *Onecut1*, *Ccl3*, *AA414992*, *Upk1b*, *H2-Q7*, and *Pcdhb2*) and 1 downregulated gene (*Eomes*) were similarly differentially expressed in our dataset (**Table S5**), indicating that 30.4% of the DEGs in the Hahn dataset[39] were also identified in our analysis. This overlap was statistically significant (Fisher's exact test using all commonly expressed genes [n = 20960] between our study and Hahn et al.'s study as the background [up: p-value = 2.3e−22, down: p-value = 0.011]). Of note, the hippocampal samples in Hahn et al.[39] are divided into the anterior/posterior regions, whereas the hippocampal samples in our study are from the whole HCP. These differences in anatomical sites could account for unique gene expression in each dataset.

To address the potential impact differences in cell type proportions between individual mice in our bulk transcriptomes, we estimated cell proportions using a cell type deconvolution algorithm. CIBERSORTx models (see the Materials and Methods section) were separately trained on two published single-cell RNA-seq datasets from young and old mouse brains encompassing 12[40] and 17 cells types[44], respectively. We used these models to impute frequency of these cell types in our bulk data (**Fig. S2C**). Both models predicted a high proportion (~90%–95%) of neurons, followed by a small portion of astrocytes (~5%). Importantly, when using the 12-cell type model trained on Ogrodnik et al.[40], we did not observe any statistically significant changes in cell type compositions between old and young mice within our samples, while a small significant change in astrocyte proportion was observed with the 17-cell type model trained on Almanzar et al. (Tabula Morris Senis, 2020)[44] (1.37% increase, adjusted p-value 0.019577). This minor increase could explain the increased inflammatory pathways found with the GSEA (see below) as expected for aged brain samples.

To complement this analysis, we performed GSEA to investigate further the cellular processes altered with age (**Table S6**). GSEA identified four major cellular processes that were altered upon age. Downregulated genes were enriched for cell cycle, cell signaling, and neurodevelopment processes, while upregulated genes were enriched for immune response and inflammation (**Fig. 2Cii**; **Fig. S2D**). Overall, our transcriptomic analysis confirmed an aging transcriptional signature in the aged HCP samples.

Imprinting methylation is stable during aging

Next, we investigated how aging influences the fidelity of genomic imprinting. This was made possible due to the use of reciprocal BL6xCAST crosses to discern parent-of-origin from genetic effects[25,45]. We first screened for imprinting methylation using IMPLICON: an amplicon sequencing method measuring DNA methylation at several ICRs across the genome at the nucleotide resolution with high coverage[38]. With this method, we are also able to separate out paternal from maternal reads based on SNPs between BL6 and CAST strains that are contained in our amplicons and conserved during bisulfite conversion. IMPLICON was successfully performed on 11 imprinted clusters (10 ICRs and the exon1a promoter of *Ddc* gene) together with two unmethylated and one methylated control regions (**Fig. 3A**; **Table S7**) in HCP, CB, and lung of four young and old female mice from both F1 BL6 × CAST reciprocal crosses.

Unmethylated (*Klf4 and Sox2*) and methylated (*Prickle1*) controls showed low (<~10%) or high (>~90%) DNA methylation levels, respectively, at both maternal and paternal alleles for all tissues analyzed (**Fig. S3A**; **Table S7**), irrespective of age. Importantly, DNA methylation at all ICRs analyzed was stably maintained with age in the HCP, CB, and lung (**Table S7**). This is illustrated for the maternally methylated *Peg3* and *Plagl1* loci (**Fig. 3Bii,3Cii**), which showed > 90% DNA methylation of the maternal allele and < 10% DNA methylation of the paternal allele, irrespective of the genetic background (**Fig. S3B**).

We also examined DNA methylation consistency between individual CpGs along individual reads using the IMPLICON method. Reads were either fully unmethylated or methylated depending on their parent of origin, independent of the genetic background. This is exemplified for *Peg3* and *Plagl1* ICRs in HCP (**Fig. 3Biii, 3Ciii**). Taking advantage of the single nucleotide resolution of IMPLICON, we also determined methylation levels at each CpG within each genomic region with aging but did not observe consistent and meaningful differences in the various tissues across aging (**Fig. S3C**; **Table S6**).

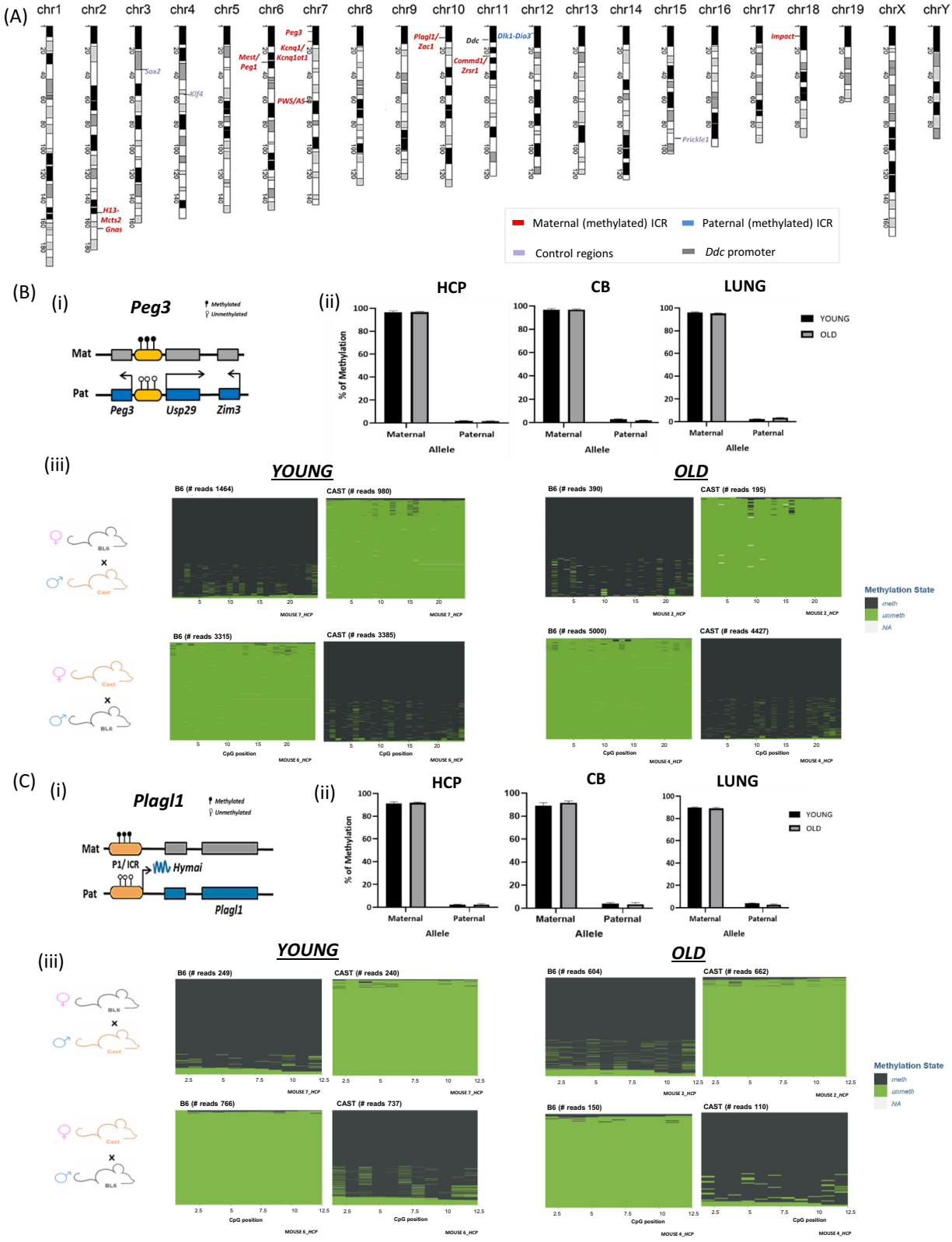

Figure 3. IMPLICON reveals methylation stability at imprinted loci in the aging brain. (A) Schematic view of the murine karyotype depicting the location of the regions studied by IMPLICON. Red and blue letters mark imprinted regions with maternally inherited and paternally inherited methylation, respectively, and violet and gray letters mark control regions and Dopa decarboxylase (*Ddc*) promoter, respectively. **(B and C)** IMPLICON analysis of **(B)** *Peg3* and **(C)** *Plagl1* imprinted clusters in HCP, CB, and lung of four juvenile and four old F1 female mouse hybrids of C57Bl/6 J (BL6) and Cast/EiJ (CAST) reciprocal crosses (two animals of each reciprocal cross per age group) measured by IMPLICON. Scheme on the left of each graph represents the expected methylation status of each region. White lollipops, unmethylated CpGs; black lollipops, methylated CpGs; gray box, non-expressed gene; blue

(legend continued on next page)

box, paternally expressed gene; Mat, maternal allele; Pat, paternal allele; regions are not drawn to scale. **(i)** Schematic representation not drawn to scale of the *Peg3* and *Plagl1* imprinted clusters for *Plagl1*, in the scheme *Hymai* noncoding RNA is also represented, being an exon gene with the transcription starting site from the same ICR promoter. **(ii)** Barplots represent the mean ± SEM methylation levels measured at each CpG within different genomic regions per parental allele in F1 female mice for CB, HCP, and lung. **(iii)** Descriptive plots displaying methylated (gray) and unmethylated CpGs (green) for each CpG position (in columns) in all the individual reads (in rows) for both the ICR of both *Peg3* and *Plagl1* imprinted loci in the HCP of two young and two old female mice from each reciprocal cross; NA, means not applicable, when methylation status was not retrieved.

Using IMPLICON, we also checked the methylation levels of the *Dopa decarboxylase* (*Ddc)* gene, which is involved in dopamine biosynthesis, and often dysregulated in neurodegenerative and psychiatric disorders[49]. *Ddc* transcripts are generally expressed from both parental alleles in most of the body tissues and can also exhibit isoform-, cell-, and development-specific imprinted expression, including in the brain[50,51]. In our samples, the exon1a promoter of the imprinted gene isoform of *Ddc* was not differentially methylated between the parental alleles, nor throughout aging, in HCP and CB, with methylation levels in two brain areas being lower than in the lung (~50% vs. 90%) (**Fig. S3Aiii**).

Finally, we also extended our IMPLICON analysis to three additional brain regions: the nucleus accumbens, prefrontal cortex, and hypothalamus. Similar to CB and HCP, these regions also showed high fidelity of differential DNA methylation for the six imprinting clusters and the control regions analyzed (**Table S8**). In conclusion, our results suggest that imprinting methylation is stably maintained during aging for the loci and brain areas investigated in this study.

The "*Imprintome*" of the young and old HCP

We next determined the "*imprintome*" of the aging mouse HPC by taking advantage of our transcriptome dataset from F1 mice of reciprocal crosses. In total, we identified 113 genes with parental-of-origin monoallelic expression in young HCP, of which 66 were maternally and 49 were paternally expressed. These genes were located in 17 genomic regions that corresponded to known imprinted regions (**Fig. 4A,4B**; **Table S9**).

Consistent with our IMPLICON results, RNAseq analysis revealed stable imprinting expression during aging in HCP. For example, *Peg3, Usp29, Zim3,* and *Plagl1* genes are exclusively paternally expressed in young and old HCP (**Fig. 4Ci,4Cii**; **Fig. S4A,S4B**), while *Ddc*, which shows no differential methylation between the parental alleles, is expressed from both alleles in both young and old HPC (**Fig. S4C**). In contrast, its neighboring imprinted gene *Grb10* was consistently expressed from the paternal allele as expected not only in young but also in old HCP. In line with the lack of aging-specific effects on genomic imprinting, expression levels of genes implicated in imprinting maintenance such as *Dppa3*, *Trim28*, *Zfp445,* or *Zfp57* remained constant. Although there was a tendency for decreased *Zfp57* expression in old HCP, this trend was not statistically significant (**Fig. S4D**).

More globally, when comparing old versus young ASE for imprinted genes using DESeq2 method, we found four not previously reported imprinted genes (*B230209E15Rik*, *Ube2nl*, *A330076H08Rik,* and *A230057D06Rik*) showing aging-specific partial erosion of strict pattern of monoallelic expression (deviating from a maternal:paternal ratio of ~0: ~100% in young to ~25: ~75% in old HPC) (**Fig. 5A**; **Table S9**). *B230209E15Rik*, *A330076H08Rik,* and *A230057D06Rik* encode for noncoding transcripts, while the pseudogene *Ube2nl* (Ubiquitin Conjugating Enzyme E2 N Like) has 91% conservation with the gene encoding for the multi-exonicubiquitin-conjugating enzyme *E2N*. Their loss of strict monoallelic expression in old HCP had a minor impact in the overall expression level of these genes (**Fig. 5B**) but was a consistent feature of the aged HCP. All these genes are located within the Prader-Willi syndrome/Angelman syndrome (PWS/AS) imprinted cluster on chr7, with the *Ube2nl* pseudogene situated within an intron of *B230209E15Rik* (**Fig. 5C**). They are normally expressed from the paternal allele and are located between the paternally expressed *Snurf-Snrpn* gene and the proximal side of the cluster that includes *Mkrn3*, *Magel2,* and *Ndn* genes. Interestingly, it is also in the PWS/AS locus, where we find the only imprinted gene, *Mkrn3* that is downregulated in old HPC, but, in this case, does not alter its RNA allele-expression ratio (**Fig. S5A**). In conclusion, these transcriptomic data are consistent with the IMPLICON results and reveal remarkable stability of genomic imprinting in physiological aging, with the rare exception of four transcripts within the large PWS/AS imprinted cluster.

XCI in the aging brain

XCI is a dosage compensation mechanism that silences one of the two X chromosomes in female mammalian cells[31]. We used our RNAseq dataset, which includes young and old female F1 hybrid mice from reciprocal crosses, to examine the status of XCI during aging process in HCP. First, we assessed the expression levels of the long noncoding RNA *Xist* that is the master regulator of XCI. There were no differences in *Xist* levels between young and old HCP (**Fig. 6A**), consistent with reanalysis of data from Hahn et al.[39] in posterior and anterior HCP of aging female samples (**Fig. S6A**). Likewise, the expression of other noncoding genes located on the X-inactivation center, such as *Ftx*, *Jpx*, and *Tsix*, remained unchanged with aging, which contrasts with the findings of a recent single nuclei RNAseq study[36] (**Fig. S6B**). Next, we explored the ASE of *Xist* and genes on the X chromosome using BL6/CAST SNP information, to gain insights on potential effects of aging on XCI. We observed a bias toward the expression of the BL6 *Xist* allele irrespective of parental origin or age, with some variation between individual animals (**Fig. 6Bi,6Bii**; **Fig. S6C**). Increase in *Xist* expression from the BL6 allele resulted in a concomitant reduction of expression from across the entire BL6 X chromosome (**Fig. 6Bi,6Bii**). This suggested a preferential inactivation of the BL6 X chromosome, which is consistent with previous findings reporting a skew toward the inactivation of the BL6 X chromosome in BL6-CAST hybrid female mice[52]. When analyzing individual genes, we observed a decrease in the percentage of BL6 reads for X-linked genes such as *Mecp2*, *Chic1*, *Atrx*, or *Huwe1* (**Fig. 6C**; **Fig. S6D**). This was a generalized behavior for all X-linked genes, which include escape genes such as *Eif2s3x* and *Kdm5c* (**Fig. S6E**). Although they can be expressed from both active and inactive X chromosomes (**Fig. S6D**), this pattern suggests that escape genes are generally more prominently expressed from the active X chromosome than from the inactive one. Some genes evade this general allelic trend across the X chromosome. For example, *Pgk1* gene, traditionally used as a biomarker of X-inactivation status[53,54], exhibits a strong preference for the expression of the CAST allele. In contrast, *Firre*, a non-coding RNA with an important role in conformational organization of

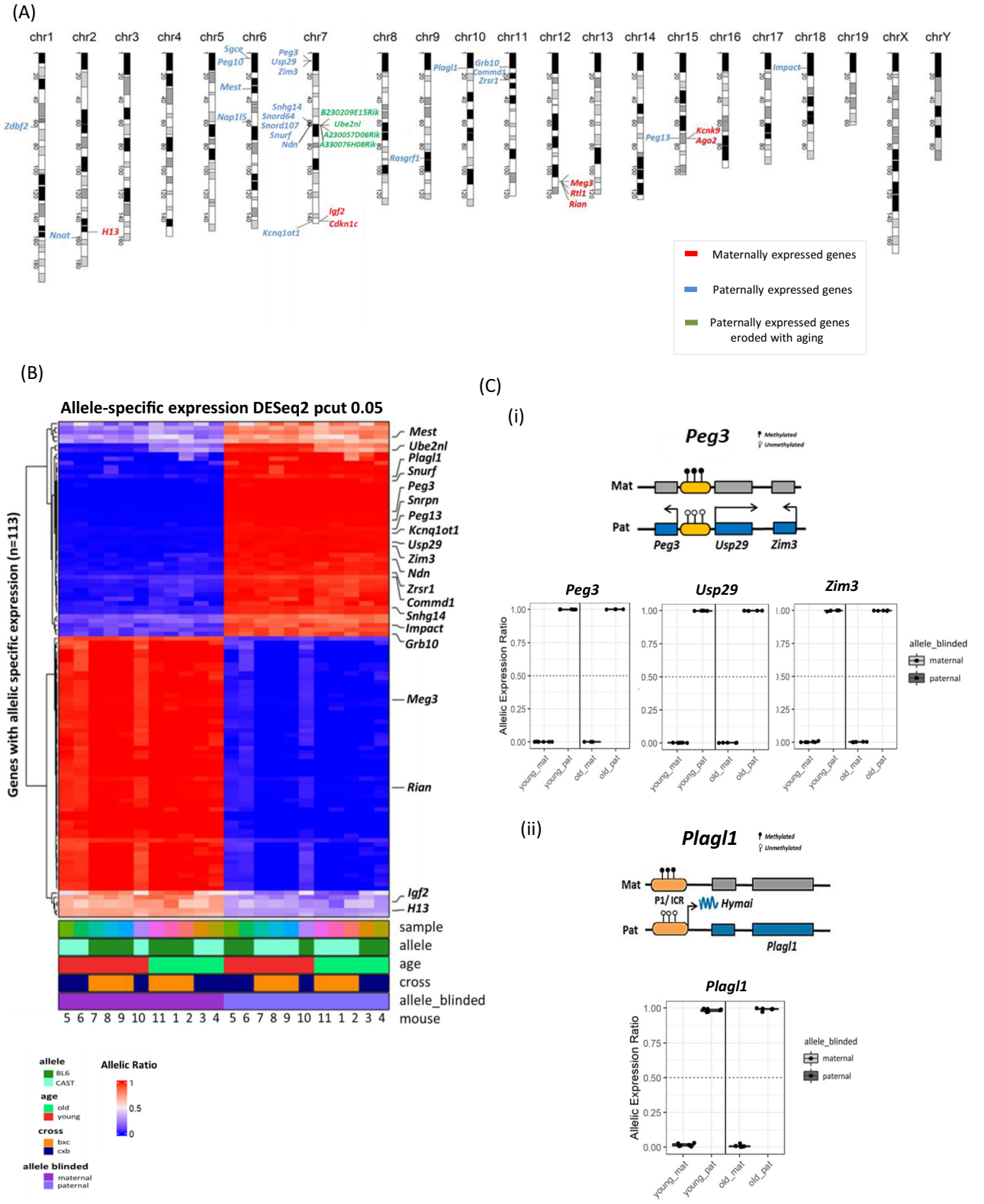

Figure 4. The "*imprintome* "of the murine HCP. (A) Schematic view of the murine karyotype depicting the location of the imprinted genes detected by RNAseq in HCP. Maternally expressed imprinted genes are marked with red, while paternally expressed imprinted genes are marked with blue. Genes marked with green are paternally expressed genes that erode with aging; for the sake of simplicity, small RNAs, such as microRNAs and snoRNAs, pseudogenes and noncoding genes of unknown function are not represented, with the exception of the genes marked with green; the full list of imprinted genes detected by RNAseq in HCP is provided in **Table S9**. **(B)** Heat map depicting the results of RNAseq transcriptomic analysis illustrating differential parental-specific gene expression of HCP in young (n = 6) and old (n = 5) female mice (F1, n = 3 young and n = 3 old mice; reciprocal cross, n = 3 young and n = 2 old mice). Color corresponds to per-gene allelic expression scores (maternal counts/total allelic counts), which are between 0 and 1,

(legend continued on next page)

scores > 0.5 (red) or < 0.5 (blue) represent genes with a maternal or paternal expression bias, whereas those with ~0.5 represent genes with bi-allelic expression. Only genes were hierarchically clustered based on these allelic ratios using euclidean distance and ward D2-based clustering. The scales on the bottom show the color codes for allelic expression levels. Examples of genes with maternal or paternal allelic expression biases are annotated on the right side of the heatmap. **(C)** Boxplot representing median ASE of the parental allele of the **(i)** *Peg3, Usp29*, and *Zim3* and **(ii)** *Plagl1*, imprinted genes in the HCP of young (n = 6) and old (n = 5) female mice measured by RNAseq (DESeq2, *P* adj < 0.05, log2FC > 1). Boxplot boundaries indicate the lower (first) and upper (third) quartiles of allele expression ratios, with the middle line indicating the median value. Scheme on top of each graph represents the expected methylation status of *Peg3* and *Plagl1* imprinted regions. White lollipops, unmethylated CpGs; black lollipops, methylated CpGs; gray box, non-expressed gene; blue box, paternally expressed gene; Mat, maternal allele; Pat, paternal allele; regions are not drawn to scale.

the Xi[55,56], exhibited strong BL6 biased expression (**Fig. S6E**). Finally, as a proxy for relaxation of XCI, we measured whether there was any increase in gene activity from the X chromosome. There was a marginal but not statistically significant increase (*Padj* = 0.51) in the proportion of reads mapping to the X chromosome in aged HCP, consistent with what we observed for individual X-linked genes (**Fig. 6D**; **Fig. S6B**). Overall, our results suggest that XCI is stable, with no signs of exacerbated skewing nor Xi relaxation, during physiological aging of the HCP.

Discussion

In this study, we present the first allele-specific epigenetic and transcriptional landscape of the aging mouse brain, with a specific emphasis on the HCP. Using a combination of IMPLICON and RNA sequencing analyses, our findings highlight the preservation of genomic imprinting and the stability of XCI throughout the natural aging process in the murine brain.

An epigenetic signature of aging has been implicated in the irreversible decline of organismal fitness and the onset of aging-related illnesses[57]. Notably, epigenetic modifications, including DNA methylation, undergo predictable changes over time, enabling the estimation of biological age based on DNA methylation "*epigenetic clocks*"[58]. Whether these epigenetic-induced changes affect maintenance of monoallelic expression including genomic imprinting and XCI was not known and thus was the focus of this study.

One typical epigenetic feature associated with the aging brain is the increase in 5hmC levels over time[59]. Indeed, 5hmC levels increase markedly during lifespan, suggesting that 5hmC-mediated epigenetic modification may be critical in neurodevelopment and neurodegenerative disorders[60,61]. Our data confirmed that 5hmC levels are higher in the brain than in peripheral tissues and increases in the HCP with age, irrespective of biological sex[60,62] (**Fig. 2A**; **Fig. S1A**). Previous studies have similarly reported age-associated increases in 5hmC in CB[63–65]. In our study, we report a trend toward increased 5hmC levels in CB, but it was not statistically significant, potentially due to the small number of CB samples analyzed (**Fig. 2A**; **Table S1**). In the HCP, the observed increased 5hmC signal during aging occurred in the absence of any changes in 5mC levels, suggesting that 5hmC may be acting as an epigenetic marker rather than an intermediary in DNA demethylation[19]. Why 5hmC levels increase during aging in the brain is not yet fully understood. One hypothesis may be that 5hmC levels increase as a compensatory mechanism in response to age-induced changes due to cellular stress in the brain's microenvironment[66,67]. Increased 5hmC levels are generally associated with the enhanced activity of Tet dioxygenases[65]; however, expression level of these enzymes in HCP did not change over time, consistent with previous studies[68]. This suggests that the increase in 5hmC may not rely on expression levels but perhaps be driven by altered enzymatic activity[67]. One interesting observation from our study was a decrease in *Uhrf1* transcript levels during aging. While Uhrf1 is primarily associated with the recognition and maintenance of 5mC during DNA replication, it can also interact with 5hmC and influence the recruitment of DNA methyltransferases[48,69]. Interestingly, previous research has demonstrated that loss of Uhrf1 leads to a global increase in 5hmC levels[47]. However, the specific mechanism underlying this differential regulation between Uhrf1 and 5hmC remains unclear and requires further investigation.

Our transcriptome analysis identified both up- and downregulated transcripts in the aged HCP. Notably, we found higher expression of genes related to inflammation and immune responses, while genes involved in cellular cycle progression, neurodevelopmental processes, and active signaling pathways displayed reduced expression levels (**Fig. 2Cii**; **Fig. S2B**). As previously reported[70,71], the upregulation of inflammatory pathways[68] and the downregulation of genes involved in pathways of growth factor signaling, encoding mitochondrial proteins and protein synthesis machinery[71] are common characteristics of aging in the brain. Interestingly, we observed canonical Wnt (Wnt/β-catenin) signaling to be dysregulated with aging. Increasing evidence indicates that Wnt signaling regulates multiple aspects of adult hippocampal neurogenesis[72] as well as neural function and synaptic connectivity[73] and downregulation of Wnt signaling could be involved in the cognitive decline associated with aging and Alzheimer's disease[74].

Our CIBERSORTx deconvolution analysis using two independent single-cell datasets[40,44] (**Fig. S2C**) revealed that the neural population of our hippocampal samples was notably high (~90%–95%) and did not vary in proportion between young and old HCP. There was a small increase in astrocyte proportions when using the single-cell dataset of the aging whole brain from The Tabula Muris Consortium as the reference[44] (right panel, **Fig. S2C**). Future studies with larger datasets will enable gene expression estimations for major cell types estimated by CIBERSORTx, providing a deeper understanding of cell-type-specific gene expression changes. Together, our transcriptome analysis aligns with previous studies[36,75] and matches other aging RNAseq datasets[40,44], suggesting a consistent and generalized pattern of gene expression changes associated with aging.

Genomic imprinting is an enduring form of epigenetic inheritance established in parental germ cells and maintained throughout an organism's development[24]. In the central nervous system, imprinting is important for neurogenesis, brain function, and behavior[27] and dysregulation of imprinting results in neurodevelopmental and behavioral disorders such as PWS/AS[24,29]. In accordance, the brain, especially neurons, consistently shows a high number of expressed imprinted genes in adulthood[18,76,77]. A detailed investigation of imprinted gene expression in the aging HCP was yet to be performed, despite the previous association between imprinting methylation and hippocampal volume in aging[78]. Recent evidence suggested that imprints can be dysregulated by environmental insults during critical periods of

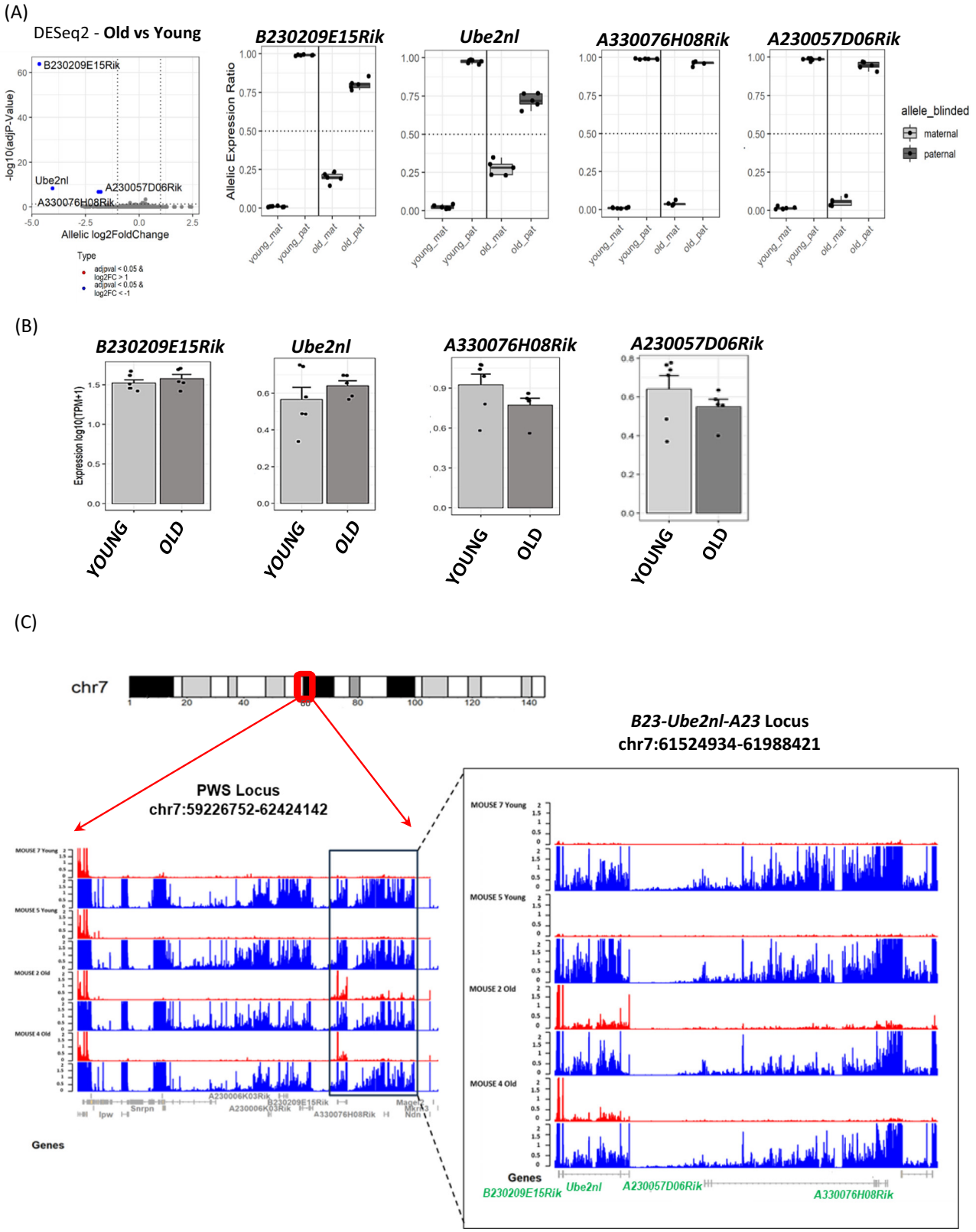

Figure 5. Loss of strict monoallelic expression of three imprinted noncoding genes within the Prader-Willi syndrome/Angelman syndrome (PWS/AS) locus. (A) On the left, dotplot detecting the allelic expression changes between young and old HPC on the newly reported imprinted genes (*B230209E15Rik*, *Ube2nl*, *A330076H08Rik,* and *A230057D06Rik*) located PWS/AS locus using DESeq2 (Wald test and BH adjustment of p-values) method comparing old versus young (P adj < 0.05, |log2FC| > 1). The log2FC represents the change in allele expression ratios between old and young mice for each gene. log2FC < −1 represents those genes that lose ASE, whereas log2FC > 1 represents those genes that have gained ASE. On the right,

(legend continued on next page)

boxplots represent the median allelic expression ratio of the parental alleles for the genes *B230209E15Rik*, *Ube2nl*, *A330076H08Rik*, and *A230057D06Rik* in young (n = 6) and old (n = 5) female HCP. Boxplot boundaries indicate the lower (first) and upper (third) quartiles of allele expression ratios, with the middle line indicating the median value. **(B)** Bulk expression levels of *B230209E15Rik*, *Ube2nl*, *A330076H08Rik,* and *A230057D06Rik* of young and old hippocampi. **(C)** Representative image of the PWS/AS locus in the mouse chr7 and RNA-seq allelic tracks representation (red = maternal, blue = paternal), two young and two old mice were chosen for display (each mouse from reciprocal cross), showing the location of the three novel imprinted genes differentially modulated in aged HCP region in square indicates the *Ube2nl/B230209E15Rik (B23)/A230057D06Rik/A330076H08Rik (A23)* locus within the PWS/AS region, where expression from the maternal allele becomes evident in the older mice.

embryonic/fetal development[79–81] with long-term consequences in tissue function and susceptibility to age-related diseases[25,76]. Whether imprinting in the brain is also susceptible to changes as a function of aging has not been addressed previously in a systematic way.

Using our allele-specific IMPLICON method, we observed a consistent DNA methylation pattern across 11 imprinted regions in the HCP, CB, and lung tissues of both young and old F1 mice as well as in their reciprocal crosses. However, we also noted that certain CpGs exhibited either increased or decreased methylation. Whether this is attributed to experimental noise or indeed has biological meaning would require further investigation. Because IMPLICON used bisulfite treatment, it cannot distinguish between 5mC and 5hmC, and so we were unable to address the potential impact of the aging-specific increase in 5hmC on imprinted regions. To tease apart 5mC and 5hmC levels at imprinting or other regions, novel techniques can now be applied such as Tet-assisted bisulfite sequencing (TAB-seq)[82] and oxidative bisulfite sequencing (oxBS-seq)[83] or emerging direct detection and single-cell methods[82] to start addressing the potential role of 5hmC at imprinted regions during aging.

We also assessed age-related allele-specific transcriptional changes in the HCP in our RNAseq dataset, documenting 113 coding and non-coding genes with parental allelic expression in the HCP across aging. In line with our IMPLICON findings, imprinted gene expression remained stable throughout the aging process. While we cannot rule out dysregulation of imprinting in the context of age-onset diseases or following environmental insults[84,85], our findings show stable parental-of-origin DNA methylation and transcription at imprinted loci during physiological aging of the brain. One caveat in our analysis is the absence of single-cell resolution, which masks the existence of other imprinted genes that may exhibit cell-type-specific imprinting. This may indeed be the case of *Ddc* gene belonging to the *Grb10* imprinted locus on chr11, which we postulated to undergo transcriptional or imprinting regulation upon aging and thus influencing dopamine production[50,51,86]. Single-cell techniques, such as scRNAseq, would be required to disclose the full "*imprintome*" of HCP during aging. Bulk RNA-seq, performed by us in this study, remains the gold standard in studying global trends in monoallelic expression in a wide range of different contexts[25] due to its reproducibility, scalability, and cost effectiveness. However, it cannot uncover more subtle changes unique to specific cell types or states. Over the past few decades, the landscape of single-cell RNA-seq (scRNA-seq) methods has experienced rapid evolution with constant improvement in sensitivity, throughput, and reproducibility. For accurately quantifying ASE in single cells, well-based methods (e.g., Smart-seq2/3) have been preferred[87]. For instance, ASE quantification by scRNA-seq has been used to elucidate the degree of XCI escape across human tissues[88], the dynamics of X-chromosome silencing[89], or to unravel dosage compensation mechanisms in mammalian preimplantation development[90]. Importantly, scRNA-seq will be crucial to understand the true extent of ASE in different cell types and states[87]. Technological improvements, including long-read single-cell RNAseq, will help overcome current challenges in ASE quantification using scRNA-seq including limitations in analyzing low-abundance transcripts, sequencing drop outs, and scalability limitations. Alternatively, cell sorting of different cell populations followed by bulk RNA sequencing has the potential to reveal subtle changes in allelic expression during aging that may be specific to particular cell types. In particular, this would enable detection of allelic expression changes that occur in opposite directions in different cell types[91], which might otherwise be obscured by using whole tissue preparations as we did in this study.

Although our data strongly point for an enduring stability of genomic imprinting in the aging brain, an exception was found for four novel non-coding transcripts at the PWS/AS imprinted locus on mouse chr7 that lost strict monoallelic expression upon aging: *B230209E15Rik*, *Ube2nl*, *A330076H08Rik,* and *A230057D06Rik*. These transcripts are strongly expressed in brain tissues; however, their exact function is currently unknown. The most enigmatic of them all is *Ube2nl*, an intronless pseudogene with an open reading frame derived from the *Ube2n* (ubiquitin-conjugating enzyme E2N) gene on mouse chr10. While we observed consistent allele biases changes in the aged HCP for these genes, this did not translate into overall gene expression changes. Functional studies will be needed to understand the role of these transcripts in mouse development and aging and whether the syntenic region in humans is also sensitive to aging-specific effect on imprinting regulation.

We also investigated changes in XCI during aging process and did not observe any differences in our dataset (**Fig. 6A**) or the RNAseq dataset from Hanh et al.[39] (**Fig. S6A**). The same observation extended to other genes on the X-inactivation center, Ftx, Jpx, and Tsix which also did not change with aging (**Fig. S6B**). Our findings contrast recent single nuclei RNA sequencing results indicating unexpected Xist upregulation in the hypothalamus and to some extent in the HCP[36], although these findings were not validated by other molecular techniques, nor did it reflect overall global differences in the activity of the X chromosome. This disparity might be explained by the technical differences between bulk RNAseq protocols versus the single nuclei RNA-seq, or in the different brain regions being analyzed. For instance, in the aforementioned study, XIST upregulation was more extreme in the hypothalamus compared with the HCP. Taking advantage of our biological system, where we can discriminate the two X-chromosomes, we mined our RNAseq dataset resource to learn more about the endurance of XCI through aging. Our data revealed a skewing of XCI toward the BL6 chrX for 10 out of 11 mice (**Fig. 6Bii**), consistent with previous studies[52]. This effect was not age specific, which contrasts with the hematopoietic system for which aging-mediated enhanced skewing has been reported[33,92]. This may be explained by the differences in cell cycle turnover, which is much higher during hematopoiesis than neurogenesis. Likewise, no signs of relaxation of XCI were observed in the aging HCP (**Fig. 6D**), which contrasts with the reported, albeit very subtle, alterations observed in the

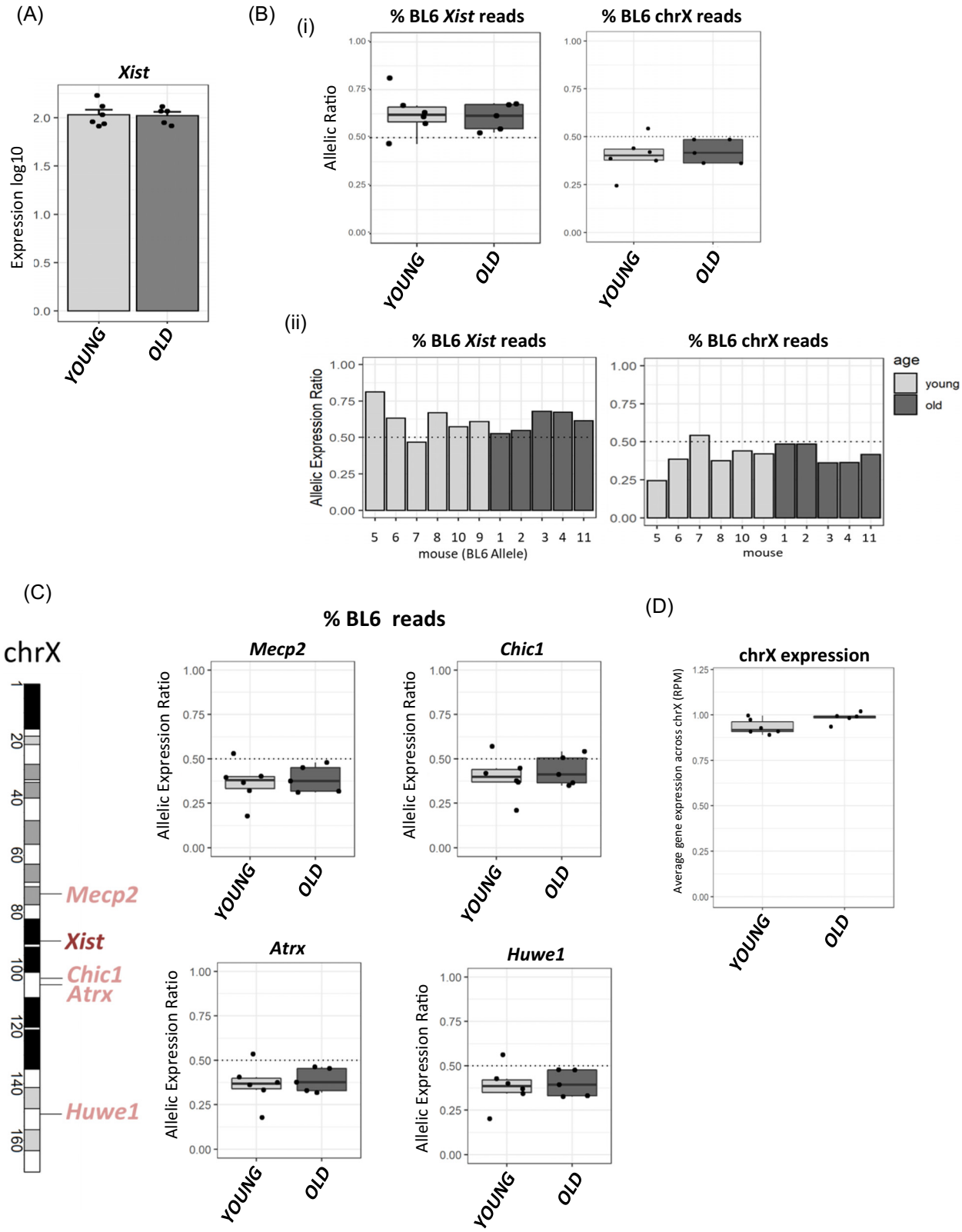

Figure 6. Stability of X-chromosome inactivation in the aged HCP. (A) Expression levels of X-inactive-specific-transcript (*Xist*) long noncoding RNA in young (n = 6) and old (n = 5) female mice in log10(TPM + 1) (transcripts per million) measured by RNAseq. **(B)** ASE ratio of *Xist* gene and the entire chrX reported as percentage of BL6 reads averaged **(i)** for young (n = 6, of which three BL6/CAST and three CAST/BL6) and old mice (n = 5, of which three BL6/CAST and two CAST/BL6) in boxplots and **(ii)** for each individual mouse. Boxplot boundaries indicate the lower (first) and upper (third) quartiles of allele expression ratios, with the middle line indicating the median value. **(C)** Median allelic expression ratio of X-linked genes; *Mecp2*, *Chic1*, *Atrx*, or *Huwe1* measured by RNAseq are represented by barplots depicting the percentage of BL6 reads. Boxplot boundaries indicate the lower

(legend continued on next page)

(first) and upper (third) quartiles of allele expression ratios, with the middle line indicating the median value. On the left, scheme of the chrX with the location of *XIST* and these genes. **(D)** Boxplot graph representing the median gene expression across chrX in reads per million (RPM) for young and old mice. Boxplot boundaries indicate the lower (first) and upper (third) quartiles of allele expression ratios, with the middle line indicating the median value.

hematopoietic system[34,35]. While it is essential to acknowledge the potential for subtle effects on XCI stability with a larger sample size, our findings unequivocally indicate that XCI is remarkable resilience to physiological aging of the HCP.

Our study represents a comprehensive investigation of the allele-specific DNA methylation and transcriptional landscape of the aging brain. While we focused on genomic imprinting and XCI, this dataset holds promise for exploring other monoallelic-specific phenomena that may be relevant to aging. We acknowledge the limitations in our study including the exclusive focus on female mice and the relatively small cohort of animals. This decision stemmed from ethical considerations and was justified as a reduced number of mice are needed when working with an isogenic setting where all animals share an identical genotype in controlled conditions. It is worth noting that although our F1 hybrid mice from reciprocal crosses could be seen as a subgroup within the young and old groups, our findings (**Figs. S1B, S3B, and S4A,S4B**) indicate that they did not differ within these age groups. Hence, we were able to have $n = 4$ young/old animals for the IMPLICON and $n >= 5$ young/old animals for the RNAseq analysis. Comparable numbers of mice have been used in similar aging studies (~5 female mice in Hahn et al.[39]). Reassuringly, our study replicated aging expression changes found in other studies (**Figs. S2C and S5A**; **Table S5**). Nonetheless, we cannot exclude that subtle or cell-specific changes in genomic imprinting and XCI might have been detected if a bigger number of animals have been analyzed. In addition, the female animals used in our study were not synchronized for the estrous cycle. Synchronization procedures are challenging to implement in long-term experiments and require increased number of animals and may introduce additional variables affecting reproducibility. Lack of synchronization for the estrous cycle is unlikely to have a major impact on the objectives of our study in elucidating the monoallelic status of genes in the aging brain as the vast majority of known imprinted genes remained strictly monoallelically expressed in all animal samples independently of their age and reciprocal cross (Fig. 4C; **Fig. S4A,B**).

In conclusion, our findings support the remarkable resilience of genomic imprinting and XCI in the face of epigenetic changes observed during healthy aging of the brain, providing advances beyond what has been previously achieved. The stability of these epigenetic processes with aging suggests their importance in preserving essential cellular functions throughout an entire individual's lifespan.

Acknowledgments

We would like to thank the members of the S.T.d.R.'s team for helpful discussions and the animal facility of the iMM for their help in maintaining the animal colonies. Work in S.T.d.R.'s team was supported by Fundação para a Ciência e Tecnologia (FCT) Ministério da Ciência, Tecnologia e Ensino Superior (MCTES), Portugal (IC&DT projects 2022.01532.PTDC and PTDC/BIA-MOL/29320/2017 as well as projects UIDB/04565/2020 and UIDP/04565/2020 of the Research Unit Institute from Bioengineering and Biosciences—iBB and LA/P/0140/2020 of the Associate Laboratory Institute for Health and Bioeconomy —i4HB) and S.T.d.R. and S.M. were supported by assistant research contracts from FCT/MCTES (2021.00660.CEECIND and CEECIND/02356.2021, respectively). Research in M.A.E.-M.'s laboratory was supported by a Snow Medical Fellowship awarded to M.A.E.-M. and the Lorenzo and Pamela Galli Medical Research Trust.

Author Contributions

S.T.d.R. conceived the study, supervised the project, and together with M.A.E.-M. secured funding. S.M. maintained the BL6 and CAST mouse lines, sacrificed the mice, dissected brain areas, performed most of the molecular biology experiments, conducted IMPLICON experiments, analyzed 5mC/5hmC measurements, IMPLICON, and RNA-seq results. J.S. prepared the RNAseq alignment, analyzed RNA-seq data, and the CYBERSORTx deconvolution analysis under the supervision of M.A.E.-M. D.O. performed the 5mC/5hmC measurements. F.K. and M.A.E.-M. conducted bioinformatic analysis of IMPLICON. A.M. helped in RNAseq, IMPLICON, and LC-MS/MS experiments. S.M. and S.T.d.R. wrote the article with contributions of J.S. and M.A.E.-M.

Conflicts of Interests

A.M. and F.K. are Altos Labs employees. The other authors declare no competing interests.

Data Availability

GEO superseries (RNAseq and IMPLICON) can be accessed here: https://www.ncbi.nlm.nih.gov/geo/query/acc.cgi?acc=GSE232548.

Supplementary Materials

Supplemental information can be found online at https://doi.org/10.59368/agingbio.20240030.

References

1. Li Y., & Tollefsbol T.O. (2016). Age-related epigenetic drift and phenotypic plasticity loss: Implications in prevention of age-related human diseases. *Epigenomics* **8**(12), 1637–1651. PMID: 27882781; doi: 10.2217/EPI-2016-0078.
2. Vijg J., & Suh Y. (2013). Genome instability and aging. *Annu. Rev. Physiol.* **75**, 645–668. PMID: 23398157; doi: 10.1146/ANNUREV-PHYSIOL-030212-183715.
3. López-Otín C., Blasco M.A., Partridge L., Serrano M., & Kroemer G. (2023). Hallmarks of aging: An expanding universe. *Cell* **186**(2), 243–278. doi: 10.1016/J.CELL.2022.11.001.
4. Pal S., & Tyler J.K. (2016). Epigenetics and aging. *Sci. Adv.* **2**(7), e1600584. doi: 10.1126/SCIADV.1600584.
5. Raj K. (2018). The epigenetic clock and aging. *Epigenetics Aging Longev.* 95–118. doi: 10.1016/B978-0-12-811060-7.00004-8.
6. Seale K., Horvath S., Teschendorff A., Eynon N., & Voisin S. (2022). Making sense of the ageing methylome. *Nat. Rev. Genet.* **23**(10), 585–605. PMID: 35501397; doi: 10.1038/S41576-022-00477-6.

7. de Witte L.D., Wang Z., Snijders G.L.J.L., Mendelev N., Liu Q., Sneeboer M.A.M., … Haghighi F. (2022). Contribution of age, brain region, mood disorder pathology, and interindividual factors on the methylome of human microglia. *Biol. Psychiatry* **91**(6), 572–581. PMID: 35027166; doi: 10.1016/J.BIOPSYCH.2021.10.020.
8. Hannon E., Lunnon K., Schalkwyk L., & Mill J. (2015). Interindividual methylomic variation across blood, cortex, and cerebellum: Implications for epigenetic studies of neurological and neuropsychiatric phenotypes. *Epigenetics* **10**(11), 1024. PMID: 26457534; doi: 10.1080/15592294.2015.1100786.
9. Luo C., & Ecker J.R. (2015). Exceptional epigenetics in the brain. *Science* **348**(6239), 1094. PMID: 26045424; doi: 10.1126/SCIENCE.AAC5832.
10. Tognini P., Napoli D., & Pizzorusso T. (2015). Dynamic DNA methylation in the brain: A new epigenetic mark for experience-dependent plasticity. *Front. Cell Neurosci.* **9**, 331. doi: 10.3389/FNCEL.2015.00331.
11. Pidsley R., Viana J., Hannon E., Spiers H., Troakes C., Al-Saraj S., … Mill J. (2014). Methylomic profiling of human brain tissue supports a neurodevelopmental origin for schizophrenia. *Genome Biol.* **15**(10), 483. doi: 10.1186/S13059-014-0483-2.
12. Lang A.-L., Eulalio T., Fox E., Yakabi K., Bukhari S.A., Kawas C.H., … Montine T.J. (2022). Methylation differences in Alzheimer's disease neuropathologic change in the aged human brain. *Acta Neuropathol. Commun.* **10**(1), 174. doi: 10.1186/s40478-022-01470-0.
13. Min S., Xu Q., Qin L., Li Y., Li Z., Chen C., … Tang B. (2022). Altered hydroxymethylome in the substantia nigra of Parkinson's disease. *Hum. Mol. Genet.* **31**(20), 3494–3503. PMID: 35661211; doi: 10.1093/HMG/DDAC122.
14. Kim B., Vasanthakumar A., Li Q.S., Nudelman K.N.H., Risacher S.L., Davis J.W. , … Alzheimer's Disease Neuroimaging Initiative (ADNI) (2022). Integrative analysis of DNA methylation and gene expression identifies genes associated with biological aging in Alzheimer's disease. *Alzheimers Dement. (Amst)* **14**(1), e12354. doi: 10.1002/DAD2.12354.
15. Huynh J.L., Garg P., Thin T.H., Yoo S., Dutta R., Trapp B.D., … Casaccia P. (2014). Epigenome-wide differences in pathology-free regions of multiple sclerosis-affected brains. *Nat. Neurosci.* **17**(1), 121–130. PMID: 24270187; doi: 10.1038/NN.3588.
16. Kato T., & Iwamoto K. (2014). Comprehensive DNA methylation and hydroxymethylation analysis in the human brain and its implication in mental disorders. *Neuropharmacology* **80**, 133–139. PMID: 24389572; doi: 10.1016/J.NEUROPHARM.2013.12.019.
17. Xu Y., Zhong L., Wei H., Li Y., Xie J., Xie L., … Lin L. (2022). Brain region- and age-dependent 5-hydroxymethylcytosine activity in the non-human primate. *Front. Aging Neurosci.* **14**, 934224. doi: 10.3389/FNAGI.2022.934224/FULL.
18. Qureshi I.A., & Mehler M.F. (2018). Epigenetic mechanisms underlying nervous system diseases. *Handb. Clin. Neurol.* **147**, 43. PMID: 29325627; doi: 10.1016/B978-0-444-63233-3.00005-1.
19. Szulwach K.E., Li X., Li Y., Song C.-X., Wu H., Dai Q., … Jin P. (2011). 5-hmC-mediated epigenetic dynamics during postnatal neurodevelopment and aging. *Nat. Neurosci.* **14**(12), 1607–1616. PMID: 22037496; doi: 10.1038/NN.2959.
20. da Rocha S.T., & Gendrel A.V. (2019). The influence of DNA methylation on monoallelic expression. *Essays Biochem.* **63**(6), 663–676. PMID: 31782494; doi: 10.1042/EBC20190034.
21. Huang W.C., Bennett K., & Gregg C. (2018). Epigenetic and cellular diversity in the brain through allele-specific effects. *Trends Neurosci.* **41**(12), 925–937. PMID: 30098802; doi: 10.1016/J.TINS.2018.07.005.
22. Jaenisch R., & Bird A. (2003). Epigenetic regulation of gene expression: How the genome integrates intrinsic and environmental signals. *Nat. Genet.* **33**(Suppl. 2), 245–254.
23. O'brien E.K., & Wolf J.B. (2019). Evolutionary quantitative genetics of genomic imprinting. *Genetics* **211**(1), 75–88. PMID: 30389806; doi: 10.1534/GENETICS.118.301373.
24. Tucci V., Isles A.R., Kelsey G., Ferguson-Smith A.C., Tucci V., Bartolomei M.S., … Ferguson-Smith A.C. (2019). Genomic imprinting and physiological processes in mammals. *Cell* **176**(5), 952–965. PMID: 30794780; doi: 10.1016/J.CELL.2019.01.043.
25. Perez J.D., Rubinstein N.D., Fernandez D.E., Santoro S.W., Needleman L.A., Ho-Shing O., … Dulac C. (2015). Quantitative and functional interrogation of parent-of-origin allelic expression biases in the brain. *Elife* **4**, 41. doi: 10.7554/ELIFE.07860.
26. Gregg C., Zhang J., Weissbourd B., Luo S., Schroth G.P., Haig D., & Dulac C. (2010). High-resolution analysis of parent-of-origin allelic expression in the mouse brain. *Science* **329**(5992), 643–648. PMID: 20616232; doi: 10.1126/SCIENCE.1190830.
27. Kishino T. (2006). Imprinting in neurons. *Cytogenet. Genome Res.* **113**(1–4), 209–214. PMID: 16575182; doi: 10.1159/000090834.
28. Higgs M.J., Hill M.J., John R.M., & Isles A.R. (2022). Systematic investigation of imprinted gene expression and enrichment in the mouse brain explored at single-cell resolution. *BMC Genomics* **23**(1), 754. PMID: 36384442; doi: 10.1186/S12864-022-08986-8.
29. Horsthemke B., & Wagstaff J. (2008). Mechanisms of imprinting of the Prader-Willi/Angelman region. *Am. J. Med. Genet. Part A* **146**(16), 2041–2052. doi: 10.1002/ajmg.a.32364.
30. Lyon M.F. (1961). Gene action in the X-chromosome of the mouse (Mus musculus L.). *Nature* **190**(4773), 372–373. doi: 10.1038/190372a0.
31. Raposo A.C., Casanova M., Gendrel A.V., & da Rocha S.T. (2021). The tandem repeat modules of Xist lncRNA: A Swiss army knife for the control of X-chromosome inactivation. *Biochem. Soc. Trans.* **49**(6), 2549–2560. PMID: 34882219; doi: 10.1042/BST20210253.
32. Peeters S.B., Yang C., & Brown C.J. (2016). Have humans lost control: The elusive X-controlling element. *Semin. Cell Dev. Biol.* **56**, 71–77. PMID: 26849907; doi: 10.1016/J.SEMCDB.2016.01.044.
33. Roberts A.L., Morea A., Amar A., Zito A., El-Sayed Moustafa J.S., Tomlinson M., … Small K.S. (2022). Age acquired skewed X chromosome inactivation is associated with adverse health outcomes in humans. *Elife* **11**, e78263. doi: 10.7554/ELIFE.78263.
34. Grigoryan A., Pospiech J., Krämer S., Lipka D., Liehr T., Geiger H., … Florian M.C. (2021). Attrition of X chromosome inactivation in aged hematopoietic stem cells. *Stem Cell Rep.* **16**(4), 708–716. PMID: 33798450; doi: 10.1016/J.STEMCR.2021.03.007.
35. Liu Y., Sinke L., Jonkman T.H., Slieker R.C., Daxinger L., & Heijmans B.T. (2023). The inactive X chromosome accumulates widespread epigenetic variability with age. *Clin. Epigenetics* **15**(1), 135. PMID: 37626340; doi: 10.1186/S13148-023-01549-Y.
36. Hajdarovic K.H., Yu D., Hassell L.A., Evans S.A., Packer S., Neretti N., & Webb A.E. (2022). Single-cell analysis of the aging female mouse hypothalamus. *Nat. Aging* **2**(7), 662–678. PMID: 36285248; doi: 10.1038/S43587-022-00246-4.
37. Paxinos G., & Franklin K.B.J. (1997). *The Mouse Brain in Stereotaxic Coordinates*. San Diego, CA: Academic Press.
38. Klobučar T., Kreibich E., Krueger F., Arez M., Pólvora-Brandão D., von Meyenn F., … Eckersley-Maslin M. (2020). IMPLICON: An ultra-deep sequencing method to uncover DNA methylation at imprinted regions. *Nucleic Acids Res.* **48**(16), E92–E92. doi: 10.1093/NAR/GKAA567.
39. Hahn O., Foltz A.G., Atkins M., Kedir B., Moran-Losada P., Guldner I.H., … Wyss-Coray T. (2023). Atlas of the aging mouse brain reveals white matter as vulnerable foci. *Cell* **186**(19), 4117–4133.e22. PMID: 37591239; doi: 10.1016/J.CELL.2023.07.027.
40. Ogrodnik M., Evans S.A., Fielder E., Victorelli S., Kruger P., Salmonowicz H., … Jurk D. (2021). Whole-body senescent cell clearance alleviates age-related brain inflammation and cognitive impairment in mice. *Aging Cell* **20**(2), e13296. doi: 10.1111/ACEL.13296.
41. Hao Y., Stuart T., Kowalski M.H., Choudhary S., Hoffman P., Hartman A., … Satija R. (2023). Dictionary learning for integrative, multimodal and scalable single-cell analysis. *Nat. Biotechnol.* **42**(2), 293–304. doi: 10.1038/s41587-023-01767-y.
42. Methi A., Islam M.R., Kaurani L., Methi A., Islam M.R., Kaurani L., … Fischer A. (2024). A single-cell transcriptomic analysis of the mouse hippocampus

after voluntary exercise. *Mol Neurobiol.* **61**(8), 5628–5645. doi: 10.1007/S12035-023-03869-9.

43. Newman A.M., Steen C.B., Liu C.L., Gentles A.J., Chaudhuri A.A., Scherer F., … Alizadeh A.A. (2019). Determining cell type abundance and expression from bulk tissues with digital cytometry. *Nat. Biotechnol.* **37**(7), 773–782. doi: 10.1038/s41587-019-0114-2.
44. Almanzar N., Antony J., Baghel A.S., Bakerman I., Bansal I., Barres B.A., … Sonnenburg J. (2020). A single-cell transcriptomic atlas characterizes ageing tissues in the mouse. *Nature* **583**(7817), 590–595. doi: 10.1038/S41586-020-2496-1.
45. Xie W., Barr C.L., Kim A., Yue F., Lee A.Y., Eubanks J., … Ren B. (2012). Base-resolution analyses of sequence and parent-of-origin dependent DNA methylation in the mouse genome. *Cell* **148**(4), 816–831. PMID: 22341451; doi: 10.1016/J.CELL.2011.12.035.
46. Jessop P., & Toledo-Rodriguez M. (2018). Hippocampal TET1 and TET2 expression and DNA hydroxymethylation are affected by physical exercise in aged mice. *Front. Cell Dev. Biol.* **6**, 45. doi: 10.3389/fcell.2018.00045.
47. Branco M.R., Ficz G., & Reik W. (2011). Uncovering the role of 5-hydroxymethylcytosine in the epigenome. *Nat. Rev. Genet.* **13**(1), 7–13. PMID: 22083101; doi: 10.1038/NRG3080.
48. Pan H., Jiang N., Sun S., Jiang H., Xu J., Jiang X., … Li R. (2020). UHRF1-repressed 5'-hydroxymethylcytosine is essential for the male meiotic prophase I. *Cell Death Dis.* **11**(2), 1–17. doi: 10.1038/s41419-020-2333-3.
49. Amano A., Tsunoda M., Aigaki T., Maruyama N., & Ishigami A. (2013). Age-related changes of dopamine, noradrenaline and adrenaline in adrenal glands of mice. *Geriatr. Gerontol. Int.* **13**(2), 490–496. doi: 10.1111/J.1447-0594.2012.00929.X.
50. Bonthuis P.J., Steinwand S., Huang W.-C., Stacher Hörndli C.N., Emery J., Kravitz S., … Gregg C. (2020). Dopa decarboxylase is a genetic hub of parental control over offspring behavior. *bioRxiv* **570**(20), 2020.06.23.168195. doi: 10.1101/2020.06.23.168195.
51. Sheng K.Y., Nakano T., & Yamaguchi S. (2022). A region-dependent allele-biased expression of Dopa decarboxylase in mouse brain. *Front. Cell Dev. Biol.* **10**, 1078927. doi: 10.3389/FCELL.2022.1078927.
52. Chadwick L.H., & Willard H.F. (2005). Genetic and parent-of-origin influences on X chromosome choice in Xce heterozygous mice. *Mamm. Genome* **16**(9), 691–699. PMID: 16245026; doi: 10.1007/S00335-005-0059-2/FIGURES/4.
53. Bousard A., Raposo A.C., Żylicz J.J., Picard C., Pires V.B., Qi Y., … da Rocha São T. (2019). The role of Xist-mediated Polycomb recruitment in the initiation of X-chromosome inactivation. *EMBO Rep.* **20**(10), e48019. doi: 10.15252/EMBR.201948019.
54. Chu C., Zhang Q.C., Da Rocha S.T., Flynn R.A., Bharadwaj M., Calabrese J.M., … Chang H.Y. (2015). Systematic discovery of Xist RNA binding proteins. *Cell* **161**(2), 404–416. PMID: 25843628; doi: 10.1016/J.CELL.2015.03.025.
55. Zhang S., Plummer D., Lu L., Cui J., Xu W., Wang M., … Jin F. (2022). DeepLoop robustly maps chromatin interactions from sparse allele-resolved or single-cell Hi-C data at kilobase resolution. *Nat. Genet.* **54**(7), 1013–1025. PMID: 35817982; doi: 10.1038/S41588-022-01116-W.
56. Fang H., Bonora G., Lewandowski J.P., Thakur J., Filippova G.N., Henikoff S., … Disteche C.M. (2020). Trans- and cis-acting effects of Firre on epigenetic features of the inactive X chromosome. *Nat. Commun.* **11**(1), 1–17. doi: 10.1038/s41467-020-19879-3.
57. Zampieri M., Ciccarone F., Calabrese R., Franceschi C., Bürkle A., & Caiafa P. (2015). Reconfiguration of DNA methylation in aging. *Mech. Ageing Dev.* **151**, 60–70. PMID: 25708826; doi: 10.1016/J.MAD.2015.02.002.
58. Frenk S., & Houseley J. (2018). Gene expression hallmarks of cellular ageing. *Biogerontology* **19**(6), 547–566. PMID: 29492790; doi: 10.1007/s10522-018-9750-z.
59. Kato T., & Iwamoto K. (2014). Comprehensive DNA methylation and hydroxymethylation analysis in the human brain and its implication in mental disorders. *Neuropharmacology* **80**, 133–139. PMID: 24389572; doi: 10.1016/J.NEUROPHARM.2013.12.019.
60. He B., Zhang C., Zhang X., Fan Y., Zeng H., Liu J., … Yi C. (2021). Tissue-specific 5-hydroxymethylcytosine landscape of the human genome. *Nat. Commun.* **12**(1), 1–12. doi: 10.1038/s41467-021-24425-w.
61. Kraus T.F.J., Kilinc S., Steinmaurer M., Stieglitz M., Guibourt V., & Kretzschmar H.A. (2016). Profiling of methylation and demethylation pathways during brain development and ageing. *J. Neural Transm.* **123**(3), 189–203. PMID: 26497022; doi: 10.1007/S00702-015-1469-2.
62. Lin I.H., Chen Y.F., & Hsu M.T. (2017). Correlated 5-hydroxymethylcytosine (5hmC) and gene expression profiles underpin gene and organ-specific epigenetic regulation in adult mouse brain and liver. *PLoS One* **12**(1), e0170779. doi: 10.1371/JOURNAL.PONE.0170779.
63. Dzitoyeva S., Chen H., & Manev H. (2012). Effect of aging on 5-hydroxymethylcytosine in brain mitochondria. *Neurobiol. Aging* **33**(12), 2881. PMID: 22445327; doi: 10.1016/J.NEUROBIOLAGING.2012.02.006.
64. Song C.X., Szulwach K.E., Fu Y., Dai Q., Yi C., Li X., … He C. (2011). Selective chemical labeling reveals the genome-wide distribution of 5-hydroxymethylcytosine. *Nat. Biotechnol.* **29**(1), 68. PMID: 21151123; doi: 10.1038/NBT.1732.
65. Wang J., Zhang K.X., Lu G.Z., & Zhao X.H. (2017). Research progress on 5hmC and TET dioxygenases in neurodevelopment and neurological diseases. *Yi chuan* **39**(12), 1138–1149. doi: 10.16288/J.YCZZ.17-086.
66. van den Hove D.L.A., Chouliaras L., & Rutten B.P.F. (2012). The role of 5-hydroxymethylcytosine in aging and Alzheimer's disease: current status and prospects for future studies. *Curr. Alzheimer Res.* **9**(5), 545–549. PMID: 22272626; doi: 10.2174/156720512800618008.
67. Borkowska J., Domaszewska-Szostek A., Kołodziej P., Wicik Z., Połosak J., Buyanovskaya O., … Puzianowska-Kuznicka M. (2020). Alterations in 5hmC level and genomic distribution in aging-related epigenetic drift in human adipose stem cells. *Epigenomics* **12**(5), 423–437. PMID: 32031421; doi: 10.2217/EPI-2019-0131.
68. Chen H., Dzitoyeva S., & Manev H. (2012). Effect of aging on 5-hydroxymethylcytosine in the mouse hippocampus. *Restor. Neurol. Neurosci.* **30**(3), 237–245. PMID: 22426040; doi: 10.3233/RNN-2012-110223.
69. Zupkovitz G., Kabiljo J., Kothmayer M., Schlick K., Schöfer C., Lagger S., & Pusch O. (2021). Analysis of methylation dynamics reveals a tissue-specific, age-dependent decline in 5-methylcytosine within the genome of the vertebrate aging model nothobranchiusfurzeri. *Front. Mol. Biosci.* **8**, 627143. doi: 10.3389/FMOLB.2021.627143.
70. Wang X., Patel N.D., Hui D., Pal R., Hafez M.M., Sayed-Ahmed M.M., … Michaelis E.K. (2014). Gene expression patterns in the hippocampus during the development and aging of Glud1 (Glutamate Dehydrogenase 1) transgenic and wild type mice. *BMC Neurosci.* **15**, 37. PMID: 24593767; doi: 10.1186/1471-2202-15-37.
71. Andronie-Cioara F.L., Ardelean A.I., Nistor-Cseppento C.D., Jurcau A., Jurcau M.C., Pascalau N., & Marcu F. (2023). Molecular mechanisms of neuroinflammation in aging and Alzheimer's disease progression. *Int. J. Mol. Sci.* **24**(3), 1869. doi: 10.3390/ijms24031869.
72. Arredondo S.B., Valenzuela-Bezanilla D., Mardones M.D., & Varela-Nallar L. (2020). Role of Wnt signaling in adult hippocampal neurogenesis in health and disease. *Front. Cell Dev. Biol.* **8**, 565112. doi: 10.3389/FCELL.2020.00860/BIBTEX.
73. García-Velázquez L., López-Carrasco P., & Arias C. (2022). Age-dependent changes in Wnt signaling components and synapse number are differentially affected between brain regions. *Exp. Gerontol.* **165**, 111854. doi: 10.1016/J.EXGER.2022.111854.
74. Bayod S., Felice P., Andrés P., Rosa P., Camins A., Pallàs M., & Canudas A.-M. (2015). Downregulation of canonical Wnt signaling in hippocampus of SAMP8 mice. *Neurobiol. Aging* **36**(2), 720–729. PMID: 25443287; doi: 10.1016/J.NEUROBIOLAGING.2014.09.017.
75. Ghanemi A., Yoshioka M., & St-Amand J. (2022). Mapping genetics and epigenetics to explore the pathways beyond the correlated ageing phenotype. *Genes* **13**(11), 2169. doi: 10.3390/GENES13112169.
76. Gregg C., Zhang J., Weissbourd B., Luo S., Schroth G.P., Haig D., & Dulac C. (2010). High-resolution analysis of parent-of-origin allelic expression in

the mouse brain. *Science* **329**(5992), 643–648. doi: 10.1126/science.1190830.

77. Higgs M.J., Hill M.J., John R.M., & Isles A.R. (2022). Systematic investigation of imprinted gene expression and enrichment in the mouse brain explored at single-cell resolution. *BMC Genomics* **23**(1), 754. doi: 10.1186/S12864-022-08986-8.
78. Lorgen-Ritchie M., Murray A.D., Staff R., Ferguson-Smith A.C., Richards M., Horgan G.W., … Haggarty P. (2021). Imprinting methylation predicts hippocampal volumes and hyperintensities and the change with age in later life. *Sci. Rep.* **11**(1), 943. doi: 10.1038/S41598-020-78062-2.
79. Robles-Matos N., Artis T., Simmons R.A., & Bartolomei M.S. (2021). Environmental exposure to endocrine disrupting chemicals influences genomic imprinting, growth, and metabolism. *Genes (Basel)* **12**(8), 1153. doi: 10.3390/GENES12081153.
80. Latchney S.E., Cadney M.D., Hopkins A., & Garland T. (2022). DNA methylation analysis of imprinted genes in the cortex and hippocampus of cross-fostered mice selectively bred for increased voluntary wheel-running. *Behav. Genet.* **52**(4–5), 281–297. PMID: 35988119; doi: 10.1007/S10519-022-10112-Z.
81. Van de Pette M., Abbas A., Feytout A., McNamara Gáinne , BrunoL., To W.K., Dimond A., … Fisher A.G. (2017). Visualizing changes in Cdkn1c expression links early-life adversity to imprint mis-regulation in adults. *Cell Rep.* **18**(5), 1090–1099. PMID: 28147266; doi: 10.1016/J.CELREP.2017.01.010.
82. Yu M., Hon G.C., Szulwach K.E., Song C.-X., Jin P., Ren B., & He C. (2012). Tet-assisted bisulfite sequencing of 5-hydroxymethylcytosine. *Nat. Protoc.* **7**(12), 2159–2170. PMID: 23196972; doi: 10.1038/NPROT.2012.137.
83. Booth M.J., Branco M.R., Ficz G., Oxley D., Krueger F., Reik W., & Balasubramanian S. (2012). Quantitative sequencing of 5-methylcytosine and 5-hydroxymethylcytosine at single-base resolution. *Science* **336**(6083), 934–937. PMID: 22539555; doi: 10.1126/SCIENCE.1220671.
84. Kappil M., Lambertini L., & Chen J. (2015). Environmental influences on genomic imprinting. *Curr. Environ. Heal. Rep.* **2**(2), 155–162. doi: 10.1007/S40572-015-0046-Z.
85. Dimond A., Van de Pette M., Taylor-Bateman V., Brown K., Sardini A., Whilding C., … Fisher A.G. (2023). Drug-induced loss of imprinting revealed using bioluminescent reporters of Cdkn1c. *Sci. Rep.* **13**(1), 1–14. doi: 10.1038/s41598-023-32747-6.
86. Prickett A.R., Montibus B., Barkas N., Amante S.M., Franco M.M., Cowley M., … Oakey R.J. (2021). Imprinted gene expression and function of the dopa decarboxylase gene in the developing heart. *Front. Cell Dev. Biol.* **9**, 676543. doi: 10.3389/FCELL.2021.676543.
87. Conte M.I., Fuentes-Trillo A., & Domínguez Conde C. (2024). Opportunities and tradeoffs in single-cell transcriptomic technologies. *Trends Genet.* **40**(1), 83–93. PMID: 37953195; doi: 10.1016/J.TIG.2023.10.003.
88. Tukiainen T., Villani A.C., Yen A., Rivas M.A., Marshall J.L., Satija R., … MacArthur D.G. (2017). Landscape of X chromosome inactivation across human tissues. *Nature* **550**(7675), 244–248. PMID: 29022598; doi: 10.1038/NATURE24265.
89. Pacini G., Dunkel I., Mages N., Mutzel V., Timmermann B., Marsico A., & Schulz E.G. (2021). Integrated analysis of Xist upregulation and X-chromosome inactivation with single-cell and single-allele resolution. *Nat. Commun.* **12**(1), 3638. doi: 10.1038/S41467-021-23643-6.
90. Lentini A., Cheng H., Noble J.C., Papanicolaou N., Coucoravas C., Andrews N., … Reinius B. (2022). Elastic dosage compensation by X-chromosome upregulation. *Nat. Commun.* **13**(1), 1854. doi: 10.1038/S41467-022-29414-1.
91. Ximerakis M., Lipnick S.L., Innes B.T., Simmons S.K., Adiconis X., Dionne D., … Rubin L.L. (2019). Single-cell transcriptomic profiling of the aging mouse brain. *Nat. Neurosci.* **22**(10), 1696–1708. PMID: 31551601; doi: 10.1038/S41593-019-0491-3.
92. Matteini F., Mulaw M.A., & Florian M.C. (2021). Aging of the hematopoietic stem cell niche: New tools to answer an old question. *Front. Immunol.* **12**, 1. PMID: 34858399; doi: 10.3389/FIMMU.2021.738204.